01 Sep 2013

Self-Potential Signals Generated by the Corrosion of Buried Metallic Objects with Application to Contaminant Plumes

Justin B. R. Rittgers

Andre Revil

Marios C. Karaoulis

Michael A. Mooney

et. al. For a complete list of authors, see https://scholarsmine.mst.edu/geosci_geo_peteng_facwork/1290

Recommended Citation

J. B. Rittgers et al., "Self-Potential Signals Generated by the Corrosion of Buried Metallic Objects with Application to Contaminant Plumes," *Geophysics*, vol. 78, no. 5, pp. EN65-EN82, Society of Exploration Geophysicists, Sep 2013.

The definitive version is available at https://doi.org/10.1190/GEO2013-0033.1

GEOPHYSICS, VOL. 78, NO. 5 (SEPTEMBER-OCTOBER 2013); P. EN65–EN82, 17 FIGS., 1 TABLE.
10.1190/GEO2013-0033.1

Self-potential signals generated by the corrosion of buried metallic objects with application to contaminant plumes

J. B. Rittgers[1], A. Revil[2], M. Karaoulis[1], M. A. Mooney[3], L. D. Slater[4], and E. A. Atekwana[5]

ABSTRACT

Large-amplitude (>100 mV) negative electric (self)-potential anomalies are often observed in the vicinity of buried metallic objects and ore bodies or over groundwater plumes associated with organic contaminants. To explain the physical and chemical mechanisms that generate such electrical signals, a controlled laboratory experiment was carried out involving two metallic cylinders buried with vertical and horizontal orientations and centered through and in the capillary fringe within a sandbox. The 2D and 3D self-potential (SP) data were collected at several time steps along with collocated pH and redox potential measurements. Large dipolar SP and redox potential anomalies developed in association with the progressive corrosion of the vertical pipe, although no anomalies were observed in the vicinity of the horizontal pipe. This discrepancy was due to the orientation of the pipes with the vertical pipe subjected to a significantly larger E_H gradient. Accounting for the electrical conductivity distribution, the SP data were inverted to recover the source current density vector field using a deterministic least-squares 4D (time-lapse) finite-element modeling approach. These results were then used to retrieve the 3D distribution of the redox potential along the vertical metallic cylinder. The results of the inversion were found to be in excellent agreement with the measured distribution of the redox potential. This experiment indicated that passively recorded electrical signals can be used to nonintrusively monitor corrosion processes. In addition, vertical electrical potential profiles measured through a mature hydrocarbon contaminated site were consistent with the sandbox observations, lending support to the geobattery model over organic contaminant plumes.

INTRODUCTION

The self-potential (SP) method entails the passive and usually noninvasive measurement of naturally occurring or anthropogenic perturbations to the electrical field that are generated by a variety of electrical source current mechanisms within the subsurface of the earth. As a result, the SP method has a multitude of useful applications due to its sensitivity to this variety of source mechanisms. Common source contributions to observed SP signals can include spatial gradients in hydraulic potential, temperature, electrical potential, and chemical or ionic concentrations, which result in various cross-coupled electrical source currents such as electrokinetic, thermoelectric, and electrochemical currents (see Minsley et al. [2007a, 2007b]; Sheffer [2007]; and Revil et al. [2011, 2012], for a recent updated review of SP geophysical applications). Although the electric signals associated with these various cross-coupled-flow phenomena prove to broaden the applicability of the SP method, they can also complicate the interpretation of SP signals when the physical and chemical states of the volume being investigated are often unknown.

Most recent applications of the SP method have been hydrologic investigations aimed at mapping fluid flow patterns (Bolève et al., 2007; Jardani et al., 2007a, 2008; Ikard et al., 2012), reconstructing the geometry of the water table (Birch, 1998; Jardani et al., 2009), and determining hydraulic parameters of porous media and aquifers (Maineult et al., 2008; Bolève et al., 2009; Martínez-Pagán et al.,

Manuscript received by the Editor 28 January 2013; revised manuscript received 12 April 2013; published online 28 August 2013.
[1]Colorado School of Mines, Department of Geophysics, Golden, Colorado, USA. E-mail: jrittger@mines.edu; marios.karaoulis@gmail.com.
[2]Colorado School of Mines, Department of Geophysics, Golden, Colorado, USA and Université de Savoie, ISTerre, CNRS, UMR CNRS 5275, Le Bourget du Lac, France. E-mail: arevil@mines.edu.
[3]Colorado School of Mines, Department of Civil and Environmental Engineering, Golden, Colorado, USA. E-mail: mmooney@mines.edu.
[4]Rutgers–Newark, Department of Earth and Environmental Sciences, Newark, New Jersey, USA. E-mail: lslater@andromeda.rutgers.edu.
[5]Oklahoma State University, Boone Pickens School of Geology, Stillwater, Oklahoma, USA. E-mail: estella.atekwana@okstate.edu.

2010; Revil and Jardani, 2010). Several other recent efforts have included the detection and imaging of groundwater infiltration into subsurface voids and sinkholes (Jardani et al., 2006, 2007b), investigating geothermal system and volcanic vent characteristics (Finizola et al., 2002; Byrdina et al., 2003; Revil et al., 2003, 2004; Yasukawa et al., 2005; Jardani et al., 2008; Richards et al., 2010), and the localization of hydromechanical disturbances associated with hydraulic fracturing activities and other natural or man-made seismic sources (Byrdina et al., 2003; Moore and Glaser, 2007; Crespy et al., 2008; Onuma et al., 2011; Haas et al., 2013).

In this study, we investigate the relationship between SP signals and redox potential (E_H) distributions associated with the corrosion of metallic objects within the subsurface. Previous work on this subject has various limitations, including the following: (1) only conceptually or experimentally investigating the electrochemical mechanisms that can generate large negative SP anomalies above ore bodies (Sato and Mooney, 1960; Timm and Möller, 2001) and (2) only performing inverse modeling for the location of SP source currents or dipoles (Revil et al., 2001, 2010; Mendonça, 2008). More recently, the relationship between SPs and redox potentials has focused solely on applications in mapping and assessment of contaminant plumes. SPs have been associated with redox potential gradients resulting from the biodegradation of dense non-aqueous phase liquids (Minsley et al., 2007a, 2007b), and bacteria-mediated organic-carbon oxidation processes in landfill leachates (Naudet et al., 2003, 2004, 2005; Minsley et al., 2007a, 2007b; Ntarlagiannis et al., 2007; Doherty et al., 2010; Revil et al., 2010; Fachin et al., 2012), and corroding iron bars (Castermant et al., 2008). The work presented here continues from these prior works by extending the SP technique to the quantitative reconstruction of electrochemical potential distributions within the near-field regions of electrical charge carriers within the subsurface, creating a framework for 3D time-lapse (4D) monitoring applications.

Our goal here is to demonstrate that the spatial gradient of redox potential is indeed a "forcing term" or mechanism that drives the generation of SP signals associated with the redox process. Furthermore, we show that a time-lapse gradient-based inversion of the electrical potential measurements can be used to detect and localize a corroding object via the reconstruction of the distribution of the source current density field, and that the spatial distribution of E_H can be nonintrusively retrieved via the obtained inverse model. This monitoring approach can be used to nonintrusively monitor redox processes in the subsurface as long as there are (biotic or abiotic) electronic conductors to carry a macroscopic (source) electrical current. We show support for this concept from recent measurements at a mature hydrocarbon contaminated site.

Table 1. Experiment 2 data collection: Dates and types of data. In addition, sand and water samples were taken on 11/01/2012 (upon completion of the experiment) for establishing electrical conductivity.

Time step	T1	T2	T3	T4	T5	T6
Date	9/20/12	9/28/12	10/1/12	10/4/12	10/24/12	10/31/12
Data type	2D SP	2D SP	2D SP	2D SP	2D SP	2D SP
Data type	—	—	—	—	—	3D SP
Data type	—	—	—	—	—	3D E_H
Data type	—	—	—	—	—	3D pH

MATERIALS AND METHODS

Experimental setup

This study was carried out during two phases called experiments 1 and 2, each over the course of several months. Experiment 1 was performed over several months from early to late fall of 2011 as a proof of concept, where only 2D and 3D SP data were collected at various time steps. Experiment 2 was carried out with a similar setup and procedure during the fall of 2012, where 2D surface and 3D volume E_H and pH data were collected in addition to the SP data at various time steps. During experiment 2, six 2D surface data sets were collected over the course of a 42-day period, followed by the collection of the 3D SP, electrical conductivity, and pH and E_H data at the end of the experiment (Table 1).

Figure 1 depicts the experimental setup, showing the data locations and the position of the reference electrode in all data sets. A total of 55 holes were drilled through a Plexiglas plate every 7.8 cm in an 11×5 grid and used as a template for electrode placement and manual insertion at eight elevations. Because the SP electrodes were not permanently installed throughout the tank, this plate was fitted to the tank to allow for accurate repopulation of an $11 \times 5 \times 8$ (x, y, z) data collection grid for the duration of the study (Figure 2). As shown in Figure 1, no data were collected beneath the reference electrode so as to prevent disturbing the reference potential. Similar to the work of Castermant et al. (2008), measurements were performed in an electrically insulating glass tank with inner lateral dimensions ($x = 89$ cm $\times$ $y = 44$ cm) as shown in Figures 1 and 2. The tank was filled with uniform sands to depths of 26 cm for experiment 1, and 30.5 cm for experiment 2 of the study. In experiment 1, we used a single uniform quartz sand type with a mean grain size (d_{50}) of 0.5 mm (Unimin Corporation #70 sand type), whereas in experiment 2, we used two layers of silica sands with $d_{50} = 0.5$ mm in the lower half of the tank and $d_{50} = 0.2$ mm (Unimin Corporation #30 and #70 sand types, respectively) in the upper half of the tank to increase the thickness of the capillary fringe. The porosities of the coarser and finer sands used in this study have been determined to be 0.504 and 0.473, respectively (Sakaki and Komatsu, 2007).

Two industry standard object (ISO) munitions analogs (part number 44615K466 of the McMaster-Carr catalog) were used for the metallic bodies. These ISOs have a cylindrical shape (33 mm in diameter by 102 mm in length). The outer protective oxidization layer (blackened steel) was first removed from the pipes with abrasives and then washed to allow for maximum corrosion of the pipes throughout the course of the study. The metallic pipes were placed at the same locations and orientations for experiments 1 and 2: One was oriented vertically and the other horizontally. Both pipes were centered at the phreatic surface established within the tank (Figures 1 and 2). The phreatic surface was maintained constant by adding small amounts of water, to offset evaporation, to the base of the tank through a vertical plastic tube installed prior to filling with sand. Tap water exhibiting an electrical conductivity of 278 μS/cm (0.0278 S/m) prior to mixing with the sand was used for experiment 1 to simulate a freshwater aquifer. For consistency

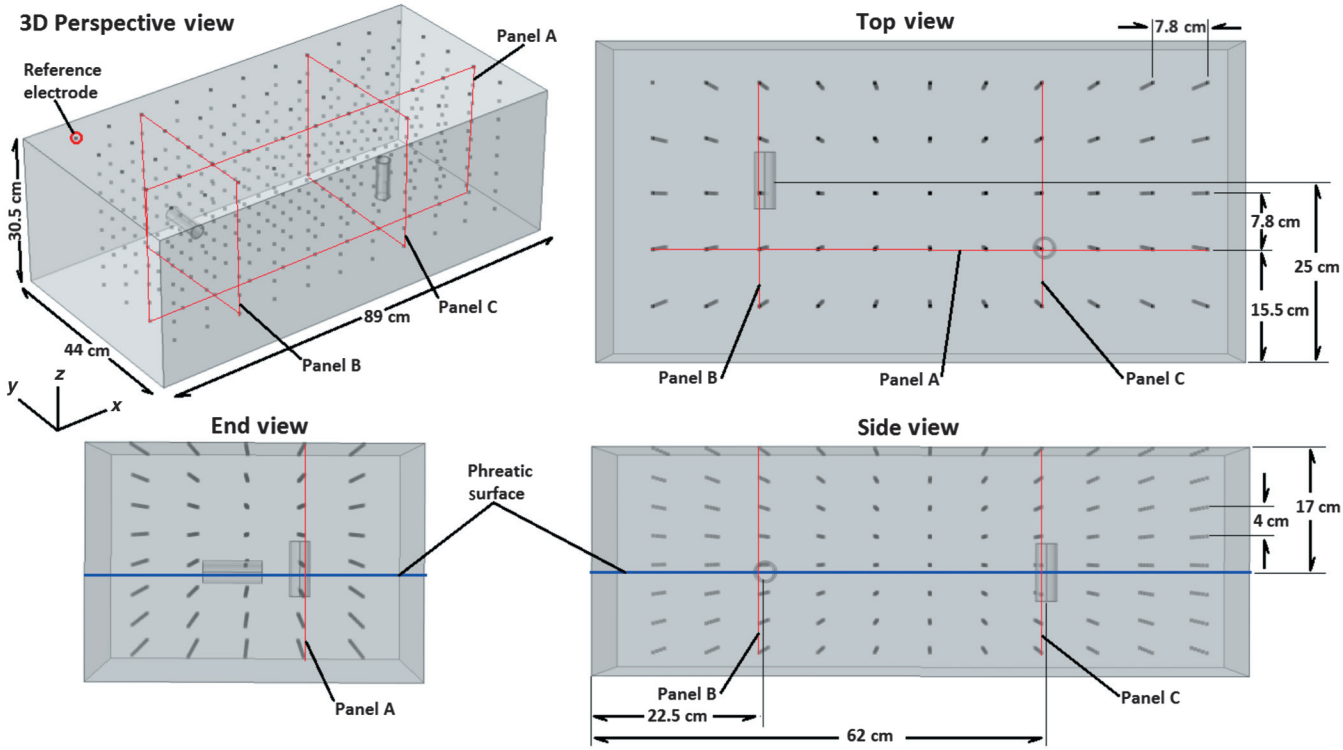

Figure 1. Sketch of the experimental setup showing the positioning of the vertical and horizontal pipes, the elevation of the established phreatic surface, the reference electrode position, the location of 3D SP data points, and the positions of 2D cross-section panels shown in the results figures.

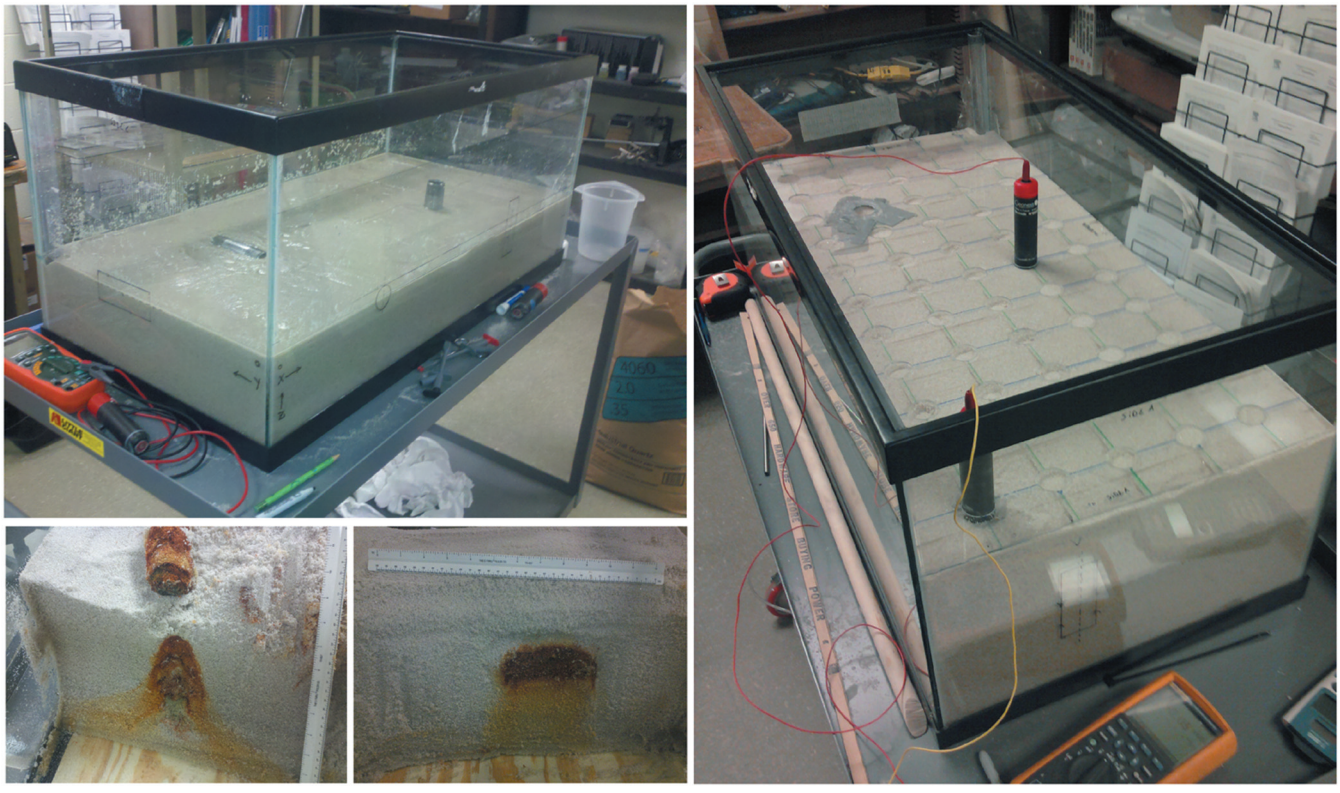

Figure 2. Photos showing the iron pipes installed during placement of sand (upper left), after placement of sand, showing Plexiglas plate and Petiau Pb/Pb/Cl electrodes (right), and excavation of pipes at the conclusion of the study, showing patterns of ferric staining of pore fluid and sand below the phreatic surface (lower left).

between the two experiments, a mixture of tap water and deionized (DI) water was used in experiment 2 to match the fluid conductivity of experiment 1. This was done because the tap water had slightly increased in conductivity. Although the initial pH of the water mixture used in experiment 2 was 7.8, the pH was not measured for experiment 1, so it is assumed that this parameter did not vary significantly between the two experiments as to alter the redox kinetics between the two tests.

Experiment

Both experiments began by first building the tank setup and then monitoring the 2D surface SP distribution for the development of any SP anomalies associated with the metal pipes. Once significant surface anomalies were observed to develop, 3D data were collected to further explore the nature of the anomalies. With the exception of beneath the reference electrode, 3D data were manually collected throughout the tank at 4-cm-depth intervals from 0- to 28-cm depth, resulting in a total of 433 measurements for the 3D SP data set collected at the end of experiment 2 (Figure 1).

For SP data acquisition, two Petiau Pb/PbCl nonpolarizing electrodes (Perrier et al., 1997; Petiau, 2000) were used for all 2D surface SP surveys. Micropellet sintered Ag/AgCl electrodes (http://www.science-products.com/Products/CatalogG/IVM-AgAgCl-Pellets/ivm.html) were used for all 3D SP measurements at depth within the tank. These micro Ag/AgCl electrodes (approximately 0.25×0.1 cm) were used to minimize the invasiveness of the 3D measurements by mounting one pellet (scanning electrode) at the end of a 1-cm-diameter plastic staff. The second electrode was placed at the predesignated reference electrode location, approximately 2 cm below the surface of the sand in the corner of the tank. The pellet-mounted staff was then used to manually probe the sand at depth throughout the tank with minimal introduction of oxygen to the system. Tip-to-tip potentials between the reference and measuring Pb/PbCl electrodes were recorded before and after each 2D surface data set was collected, and any static potential and drift was removed from the 2D data. Drift of the two micro SP electrodes was removed from the 3D data by means of a reference measurement taken after every eighth depth measurement. All SP measurements were made with a Fluke-83 multimeter exhibiting high input impedance (50 MΩ) and 0.1-mV resolution in DC volts mode. This error level was verified with several repeat measurements.

The E_H and pH data were only collected at the end of experiment 2 once the SP anomaly had developed. The pH data were collected using a Denver Instruments pH and temperature probe. Calibration standards were used several times to insure the highest measurement quality. The E_H data were collected using an InLab REDOX-L electrode in conjunction with the Denver Instruments pH meter (using relative mV mode). Drift of the redox probe and meter was removed from the E_H data by recalibrating the probe following each measurement using a relative redox potential calibration solution made of oxygen-saturated DI water. Similarly, the pH probe and meter were calibrated every eighth measurement using a 4-pH standard solution. After drift correction, the E_H data were repeatable to approximately ±10 mV, and the pH data were repeatable to within approximately ±0.1 pH unit.

Bulk electrical conductivity distribution within the tank was determined by extracting several vertical sand cores at the end of experiment 2 and performing 1D resistivity profiles. These cores were then divided into 42 individual 2-cm-long depth samples (see Figure 3), and the bulk conductivity of each sample was calculated by determining the average pore water conductivity, the water saturation of each sample, and by using Archie's law with an assumed value for the cementation exponent m equal to 1.3 for unconsolidated sands (see Ikard et al. [2012], who used the same sand). In the immediate vicinity of the iron pipes (near field), discrepancies between the true and calculated conductivity may occur because of the changes in the redox and pH conditions as well as the diffusion and sorption of ferric ions into pore fluids and sand grains from the corrosion of the metallic bars (see Figure 2). As shown in Figure 3, the determined values of electrical conductivity were then interpolated throughout the tank volume for use in the inversion of SP data. A conductivity of 1×10^3 S · m^{-1} is assumed for the iron pipes. Taking higher values can introduce instability in the finite element modeling used below.

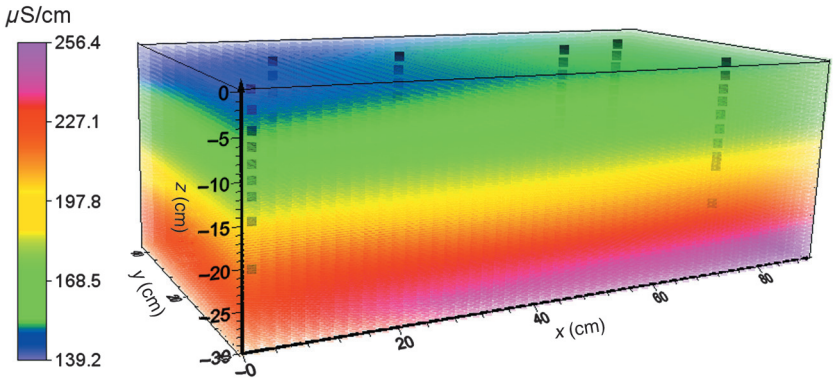

Figure 3. Bulk electrical conductivity distribution of the sand medium throughout the tank, as calculated from Archie's law for clean sands using water saturation measurements and pore fluid samples taken at the end of experiment 2 (day 42). Note the vertical and horizontal gradients in this field, resulting from the vertical variations in water saturation and subhorizontal variations in pore fluid conductivity likely due to varying ferric ion species concentrations. The 42 locations of sand core samples are shown as black squares. In units of centimeters, pore fluid samples were extracted at approximate (x, y, z) coordinate locations (0, 20, −25) (40, 35, −25) (40, 10, −30), and (80, 20, −25).

OBSERVATIONS

Electrical potential data

Figure 4 shows the conceptual relationship between water saturation and E_H as a function of depth above and below the phreatic surface within the tank. Here, dissolved atmospheric oxygen levels are assumed to dictate the trend of the background redox potential with depth. The Fe^{2+}/Fe^{3+} redox couple has a very significant effect on the redox potential profile in the tank. The E_H plot is projected onto the metallic pipes to depict the larger E_H gradient crossed by the vertical pipe in the tank. Our conceptual model assumes that the orientations of the pipes will result in a relatively large SP anomaly associated with the vertical pipe and a small anomaly or no anomaly associated with the horizontal pipe. Figures 5–7 demonstrate that our measurements support this conceptual model.

Figure 5 shows the 3D SP data collected during experiment 1 as a 3D volume with transparency thresholding for visualization. It is worth noting that the use of coarser sand during experiment 1 likely resulted in a steeper water saturation curve and therefore a stronger E_H gradient directly above the phreatic surface. This steeper E_H gradient, in combination with a lower water saturation in the upper region of the tank, resulted in a more spatially extensive and larger amplitude SP anomaly (approximately −87 mV at the surface above the vertical pipe) in comparison with the data collected during experiment 2 (approximately −55 mV at the surface above the vertical pipe) where finer-grain sand was used above the phreatic surface. The finer-grain sand caused the capillary fringe to extend further upward from the phreatic surface, steepening the water saturation curve and decreasing the E_H gradient across the metallic pipes shown in Figure 4. In experiment 2, the finer-grained sand and increased water saturation above the phreatic surface likely caused a higher bulk conductivity, resulting in the more spatially compact negative pole compared to experiment 1 (see Figures 5 and 7).

Figure 6 shows the progressive development of the negative SP anomaly located above the vertical pipe during experiment 2. On the 42nd day of experiment 2 (10/31/2012), the negative surface anomaly located above the vertical pipe was deemed to have reached an adequate signal-to-noise ratio (approximately 130 in this case), and the 3D SP data collection was conducted throughout the tank. Three vertical panels that intersect the vertical and horizontal pipes were extracted from the 3D data and plotted as a 2D cross section in Figure 7. The dipolar nature of the SP anomaly associated with the vertical pipe becomes apparent in Figure 7a and 7c, and we again see that there is virtually no SP response associated with the horizontal pipe as seen in Figure 7a and 7b.

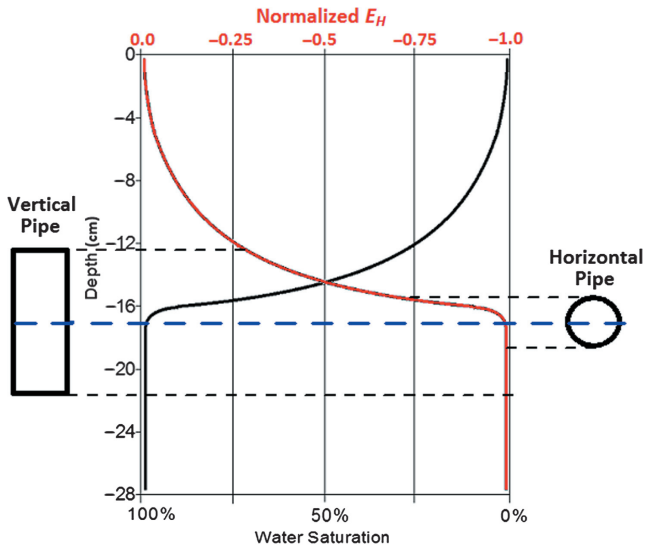

Figure 4. Sketch of the conceptual relationship between water saturation (black plot line) and E_H (red plot line) as a function of depth within undisturbed regions of the tank. The water saturation increases with depth from nearly 0% to 100% through the vadose zone due to capillary forces above the phreatic surface (blue dashed line). Conversely, the E_H is seen to decrease and become more negative with depth due to the decrease in dissolved atmospheric oxygen within the pore fluids at depth.

E_H and pH data

The day following the 3D SP data acquisition, the E_H and pH distributions were measured as well, and results are presented in Figures 8 and 9, respectively. The E_H and pH data were only collected along the vertical slices shown in Figures 8 and 9 (panels a-c for the E_H data and only panel a for the pH data). However, this data coverage was adequate to investigate the spatial distributions of E_H and pH within the tank and any perturbations to these fields within the vicinity of the pipes. These 3D SP and E_H data are used for the inverse modeling described below.

Here, we see that a large-amplitude negative E_H plume developed just around the lower half and directly below the vertical pipe (near-field perturbations), whereas a much smaller-amplitude negative E_H region developed below the horizontal pipe (Figure 8). In the far-field regions of the tank, the E_H distribution is relatively unchanged, and a gradual vertical E_H gradient is observed. Similarly, the pH data along (a) show a positive or basic pH anomaly developed near the top of the vertical pipe (Figure 9). This trend in the pH appears to be constrained by the position of the phreatic surface, suggesting that the

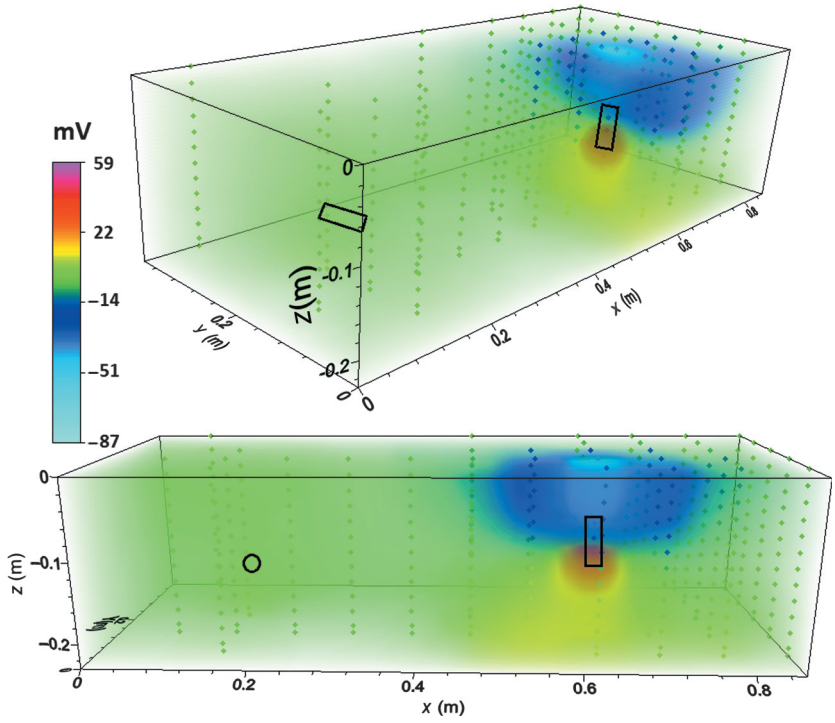

Figure 5. A 3D color contour plot with transparency thresholding of 3D SP data collected on day 105 in experiment 1. The data locations and approximate locations of the metallic pipes are shown on the plots.

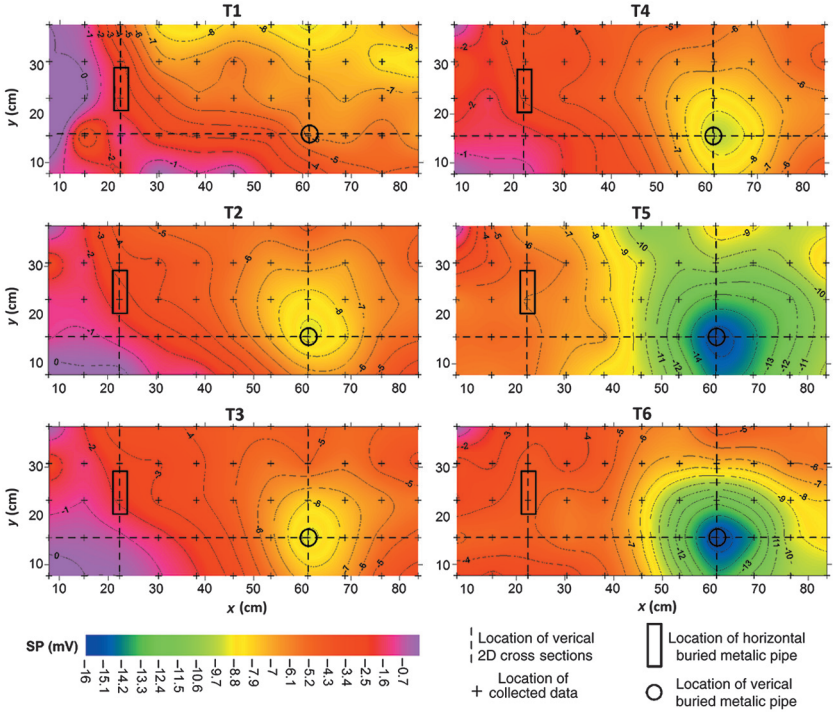

Figure 6. Sequence of 2D SP data (plan-view) collected across the surface of the sand in experiment 2. T1 to T6 denote the six snapshots.

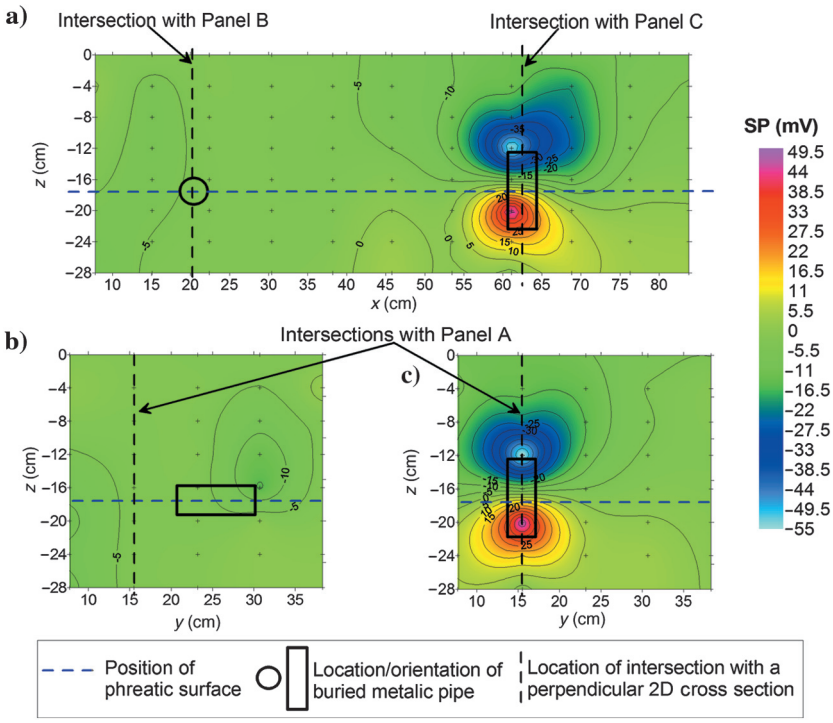

Figure 7. A subset of 3D SP data collected on day 42 of experiment 2, selected for plotting along 2D vertical cross sections. A relatively large dipolar perturbation in the electrical potential field can be seen to have developed along the vertical pipe, and a relatively small vertical dipolar perturbation is near the horizontal pipe.

reduction processes at the surface of the upper half of the vertical pipe helps to produce OH^- ions in solution above the phreatic surface. As the metallic bodies corrode, E_H further decreases below the vertical pipe while the pH increases above it, providing a positive feedback that intensifies the corrosion process. In many naturally occurring shallow subsurface environments, precluding high pH, high temperature, and high ionic concentrations, this positive feedback phenomenon will eventually be damped and counteracted over time by the formation of an electrically resistive and less reactive crust of oxides about the anodic region of the metallic body as it corrodes (see Figure 2).

Redox chemistry and corrosion

Corrosion of iron occurs in the presence of water. The reaction of iron with oxygen forms rust $Fe_2O_3.XH_2O$ where X represents the amount of water molecules complexed with the Fe (III) oxide (ferric oxide like green rust). The formation of rust starts with the oxidation of iron to ferrous ions according to $Fe \rightarrow Fe^{+2} + 2e^-$ in the lower part of the iron bar and Fe (II) ions are further oxidized to form ferric ions (Fe[III]) ions according to $Fe^{+2} \rightarrow Fe^{+3} + 1e^-$ (see Figure 10). The electrons flow in the iron bar providing the source current density $\mathbf{J}_S$. These electrons are used to reduce oxygen according to $O_2(g) + 2H_2O + 4e^- \rightarrow 4OH^-$. These OH^- ions increase the pH to basic conditions above the iron bar in agreement with the data shown in Figure 9. The formation of rust may occur away from the erosion of the iron bar. Indeed, electrons are produced via the initial oxidation of iron, and then they are driven through the metal, whereas the iron ions can diffuse through the pore water of the sand where oxygen is available. This process results in an electrochemical cell. In this electrochemical cell, iron serves as the electron donor at the anode and oxygen gas serves as the terminal electron acceptor at the cathode (Figure 10).

MODELING

The geobattery model described above is globally electroneutral by necessity, which means that the total positive pole (positive source figure of current) should exactly counterbalance the negative source (sink) of current when they are both integrated over the source/sink volumes. The result can be described as a bipole (two poles of opposite sign separated by a distance that is not necessarily negligible with respect to the distance to the observation point). When this distance is actually much bigger than the separation distance between the source and the sink of current,

the bipole is actually a dipole, and we will use this approximation below.

Our goal in this portion of the study is to apply a dipole-based inversion algorithm in an effort to recover the 3D vector distribution of source current throughout the tank for two purposes: (1) to localize the major causative sources of electrical disturbances observed in the tank (i.e., locate the vertical pipe) and (2) retrieve the 3D distribution of E_H near the vertical pipe from the SP data. This approach to modeling the data is carried out by first developing a forward model or mapping operator (kernel matrix). Three deterministic inversion approaches using Tikhonov regularization are then carried out. First, all three inversion approaches are carried out and results are compared with the aim of best localizing the metallic body, using three differing measures of the model seminorm during minimization of the solution: L1-norm, L2-norm, and a minimum support L0-norm or minimum source volume (compactness). All three inversion approaches used a robust L1-norm measure of data misfit or residual norm, which is the sum of the absolute values of the differences between the *i*th observed datum and the *i*th recovered datum. Next, inversion is performed using only an L2-norm measure of the model seminorm, to help reconstruct the smooth or diffuse distribution of E_H within the region immediately surrounding the vertical metallic pipe. It is worth noting here, that the E_H distribution is only recoverable within the far-field regions of the tank (remote locations with respect to the position of a corroding body) by means of in situ borehole measurements of E_H. In the absence of an appreciable electrical conductor that crosses the E_H gradient (e.g., a metallic body or mediating bacterial plume), there is no electron transfer, no conduction current source density, and therefore no associated measurable perturbations to the electric field. Hence, there is no way to recover the far-field redox potential distribution from the SP data alone. This is referred to as an "annihilator" in potential field theory (see the discussion in Jardani and Revil [2009] for the SP problem).

Forward modeling

The governing equation for the occurrence of SP signals is obtained by combining a constitutive equation with a continuity equation. The constitutive equation corresponds to a generalized Ohm's law for the total current density $\mathbf{J}$ (in $A \cdot m^{-2}$):

$$\mathbf{J} = \sigma \mathbf{E} + \mathbf{J}_S, \qquad (1)$$

where σ denotes DC electrical conductivity of the porous material (in $S \cdot m^{-1}$), $\mathbf{E} = -\nabla\varphi$ the electrical field in the quasistatic limit of the Maxwell equations (in $V \cdot m^{-1}$), and φ the electrical potential (in volts). As derived by Arora et al. (2007) and Linde and Revil (2007), and discussed by Castermant et al. (2008), the source current density in the metallic body can be given by $\mathbf{J}_S = -\sigma_c \nabla E_H$, where σ_c is the bulk electrical conductivity of the region or material crossing ∇E_H, which is the spatial gradient in redox potential. In our study, the electrical conductivity of the metallic pipe is used, and this simplified model assumes that redox reactions at the interface of the bar do not have a significant effect on the overall flow and exchange of electrons through the conductor. Additionally, due to the extremely conductive nature of the metallic pipe, it is assumed that the presence of any bacteria within the

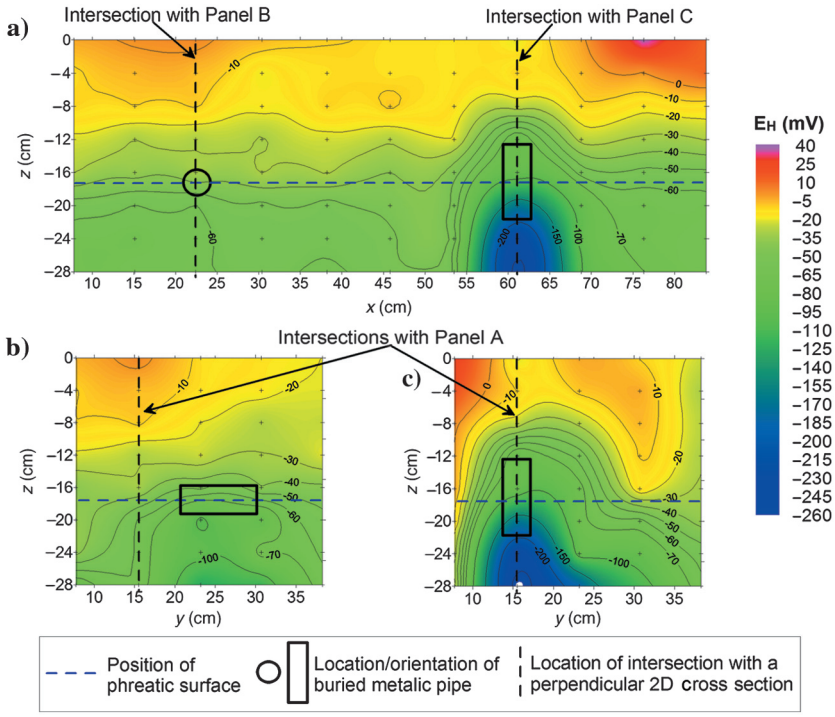

Figure 8. Redox potential (E_H) distribution. The E_H data were collected along 2D vertical cross sections within the tank at the end of experiment 2 (day 42). A relatively large negative perturbation in the E_H distribution can be seen to have developed below the vertical pipe, and a relatively small perturbation below the horizontal pipe, probably associated with the diffusion of the Fe^{2+} and Fe^{3+} ions.

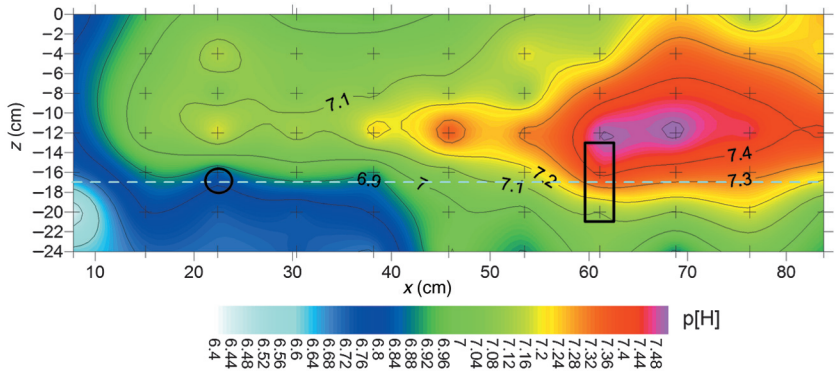

Figure 9. The pH data collected along a 2D vertical cross section (along Figure 1a) during experiment 2 (day 42). Note the basic pH recorded at the cathode of the vertically buried metallic pipe, which is consistent with the expected electrochemistry of the problem. The dashed white line denotes the position of the water table.

tank that may be mediating the corrosion process via "nanowire" appendages (Gorby et al., 2006) have little influence on the source current distributions in the immediate vicinity (near field) of the pipes. In the case of no external sources or sinks of current, equation 1 can be combined with the following conservation equation in the quasistatic limit of the Maxwell equations:

$$\nabla \cdot \mathbf{J} = 0. \tag{2}$$

Combining equations 1 and 2 yields a Poisson's equation for the SP φ (expressed in volts):

$$\nabla \cdot (\sigma \nabla \varphi) = \Im, \tag{3}$$

where $\Im$ denotes the volumetric current density (in $A \cdot m^{-3}$). This volumetric current density can be written as

$$\Im \equiv \nabla \cdot \mathbf{J}_S = \nabla\sigma \cdot \nabla \mathrm{E_H} + \sigma \nabla^2 \mathrm{E_H}. \tag{4}$$

The solution of equation 3 can be written into the following convolution integral:

$$\varphi(P) = \int_{\Omega} \mathbf{K}(P, M)\mathbf{J}_S(M)\mathrm{d}V, \tag{5}$$

where $\mathbf{K}(P, M)$ is called the kernel or the leading field (e.g., Trujillo-Barreto et al., 2004) and $\mathrm{d}V$ is a small volume around each source point M. The elements of the kernel are the Green's functions connecting the SP data at a set of measurement stations P located at the ground surface or in boreholes and the sources of current density at a set of source points located in the conducting ground. The source current density $\mathbf{J}_S$ is discretized over M elements. In our case here, the model space is discretized into $M = 1694$ elements. Each element of the discretized grid can be characterized by a small volume element $\mathrm{d}V$. The integral in equation 5 performs the superpositional summation of all contributions within the source volume or domain Ω to the measured SP at each point P. We next use this equation in our attempt to locate the position of the vertical pipe, as well as in our effort to reconstruct the $\mathrm{E_H}$ distribution along the surface of the vertical metallic pipe. The kernel computation accounts for the electrical resistivity distribution and for the insulating boundary conditions applied to the system and governed by the tank walls. In the following computations, we will use the measured and calculated resistivity distribution for the domain.

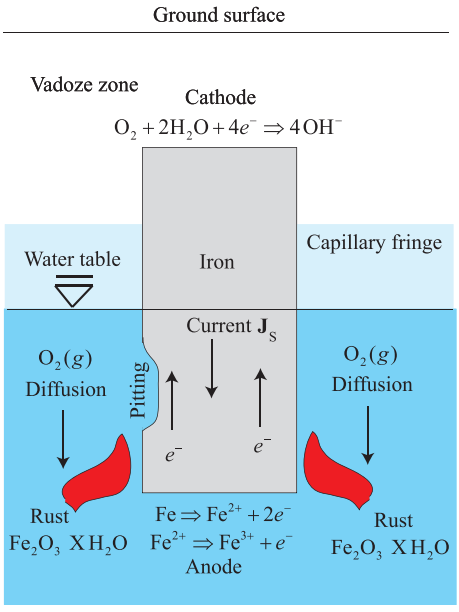

Figure 10. Galvanic cell associated with the corrosion of the iron bar. The rust is formed when the Fe^{2+} and Fe^{3+} ions (resulting from the pitting of the iron bar at the anode) meet the oxygen diffusing inside the tank from the vadose zone.

Accounting for the presence of the metallic pipes within the sand tank is crucial to maximizing the accuracy of the kernel and localization of the source currents contributing to the measured SP data. In this study, however, we assume this portion of the electrical conductivity distribution is not known in real-life situations (because it presumes that the location/extent of a metallic target or biodegraded plume is already known), so we do not account for the conductivity of the metallic pipes in the formulation of the kernel matrix used for localization, so as to represent a more realistic scenario in application. Once localization is performed, the kernel matrix is updated to account for the conductivity of the located metallic pipes, allowing for a more accurate time-lapse SP inversion and recovery of redox potential distributions. For all inversions, the full 3C ($\mathbf{J_x}$, $\mathbf{J_y}$, $\mathbf{J_z}$) current density vector field ($\mathbf{J}_S$) is reconstructed in 3D space. Because we are inverting for the 3C vector field distribution of $\mathbf{J}_S$, the total number of model parameters that are recovered in each inversion is equal to $3 \times M = 5082$. The magnitude of the recovered current density vector field is then calculated for better visualization of the results.

Static 3D and time-lapse (4D) inverse modeling

As depicted in the modeling flowcharts in Figure 11, 3D SP and 2D surface SP data are used to achieve two objectives of the study (11a and 11b, respectively). Here, we seek to localize the causative source body (Figure 11a) and also to recover or image the redox potential distribution within the near-field of the causative body (Figure 11b). For the purpose of localization, Tikhonov regularization using a classical least-squares or L2 norm approach, an L1 norm (i.e., Farquharson and Oldenburg, 1998), and compact source measures of model-norm are performed using the 3D SP data ($N = 433$) collected at the end of experiment 2. Here, it is worth noting that although we develop the general framework for the time-lapse inversion problem in this section, only a single time step of data was used and no depth weighting (discussed below) was applied for the localization step, because we are dealing with only a single 3D data set collected throughout the volume of the tank (Figure 11a). Once the localization efforts are carried out, the best solution is then selected and used to further constrain the inversion process shown in Figure 11b. To reconstruct the evolution of redox potential distributions within the tank over time, we carry out 3D time-lapse (4D) smooth-model (L2) inversion using the 2D surface SP data ($N = 55$) acquired at six time steps (Figure 11b). Last, the 2D surface SP data could be used to carry out 3D time-lapse (4D) compact-source model inversion to attempt localization of the causative body using only surface SP data. However, we save this and related efforts on improving algorithms for depth weighting of surface SP data inversion for future works.

We consider N electrodes or data points ($N = 433$ for the 3D data set, and $N = 55$ for each 2D time-lapse surface data set) and time-lapse variations of the SP field. The potential at an observation point P at a given time t is now given by

$$\varphi(P,t) = \int_{\Omega} \mathbf{K}(P,M,t)\mathbf{J}_S(M,t)\mathrm{d}V, \tag{6}$$

where the kernel $\mathbf{K}(P,M,t)$ will be considered equal to $\mathbf{K}(P,M)$ and therefore time independent (the resistivity distribution can be considered in our case to be roughly constant over time). The discretization of equation 6 for a set of N SP stations yields

$$\mathbf{y} = K\mathbf{x} + \mathbf{n}, \tag{7}$$

where $\mathbf{y}$ is the vector of potential data, K denotes the discretized form of the kernel, $\mathbf{x}$ is the vector of model parameters, and $\mathbf{n}$ is a noise vector. The same equation is obtained if true dipoles are considered. If we consider in addition T discrete time samples, we end up with the following system of linear equations:

$$\begin{bmatrix} y(r_1,1) & \cdots & y(r_1,T) \\ \vdots & \ddots & \vdots \\ y(r_N,1) & \cdots & y(r_N,T) \end{bmatrix} = \begin{bmatrix} G(r_1,r\prime_1) & \cdots & G(r_1,r\prime_p) \\ \vdots & \ddots & \vdots \\ G(r_N,r\prime_1) & \cdots & G(r_N,r\prime_p) \end{bmatrix} \times \begin{bmatrix} d_{1,1}e_1 & \cdots & d_{1,T}e_1 \\ \vdots & \ddots & \vdots \\ d_{p,1}e_p & \cdots & d_{p,T}e_p \end{bmatrix} + \begin{bmatrix} n_{1,1} & \cdots & n_{1,T} \\ \vdots & \ddots & \vdots \\ n_{N,1} & \cdots & n_{N,T} \end{bmatrix}, \tag{8}$$

$$\mathbf{Y} = \mathbf{K}\mathbf{X} + \mathbf{N}, \tag{9}$$

where $\mathbf{Y}$ is the matrix of data measurements, $\mathbf{X}$ is the matrix of dipole moments at different times, and $\mathbf{N}$ is the noise matrix. Here, we use a constant Lagrangian weighting factor to impose smoothness in structural changes between adjacent discrete time steps as opposed to the active spatiotemporal constraint techniques such as the active time constrained approach developed by Karaoulis (2011a, 2011b).

In the following, we write p the number of dipoles or equivalent current densities. Two main avenues are possible to perform the inversion of the SP data. The first possibility is to use a nonparametric optimization method, also called SP tomography. In this case, a distribution of current sources or dipoles usually makes the problem underdetermined (for example, $p = M \ll N$). This approach has been used to invert SP signals associated with ground water flow (Jardani et al., 2007a, 2007b, 2009; Minsley et al., 2007a; Bolève et al., 2009), contaminant plumes (Linde and Revil, 2007; Minsley et al., 2007b), and ore bodies (Castermant et al., 2008; Mendonça, 2008).

A second approach to invert SP data is to use a parametric inversion. In this approach, few dipoles or equivalent sources of current are assumed in the model whose location and orientation are unknown (see Haas et al. [2013], who used a combination of the two approaches). This approach is discussed in Appendix A. In geophysics, several inversion approaches have been developed along these lines, usually looking for the characteristics of a single dipole, which in 3D corresponds to three unknowns to describe the position of the dipole, two angles, and one magnitude, so it is a total of six unknown parameters per dipole. This approach is usually overdetermined or mixed determined ($p \ll N$), and the inversion is nonlinear. This parametric inversion approach is appropriate for finding the position and orientation of the metallic object in this study. However, the parametric approach recovers only a single dipolar source and doesn't allow for the retrieval of the distributed redox potential field in the vicinity of the metallic pipes. Furthermore, this approach assumes a homogeneous conductivity structure. Therefore, an SP tomography approach is carried out in this study, in which we restate the inverse problem given in equations 7 through 9 as a minimization problem partially constrained with Tikhonov regularization.

We first consider the following cost function $P^a(\mathbf{X})$ to be minimized, subject to equations 7 through 9:

$$P^{\alpha}(\mathbf{X}) = \varphi_d(\mathbf{X}) + \alpha\varphi_m(\mathbf{X}), \tag{10}$$

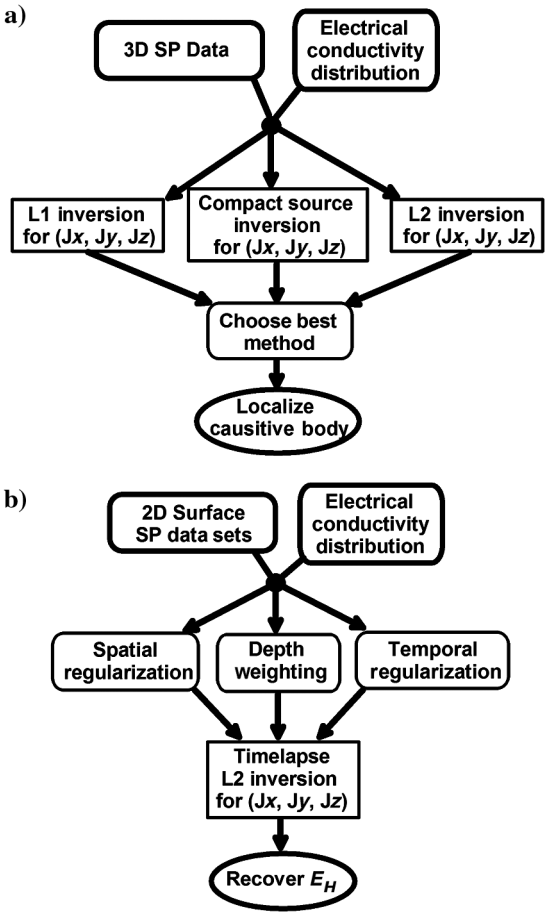

Figure 11. Flowcharts for the processing of the electrical potential data. Here, the 3D SP data are used to compare the abilities of the L1-norm, L2-norm, and compact source inversion techniques in recovering the location of the causative body. Additionally, 2D surface SP data are used in a 3D time-lapse (4D) inversion that imposes smoothness in space (L2-norm) and time (first-order derivative operator) to recover the evolution of the redox potential distribution. Here, spatial and temporal regularization terms within the objective function are formulated to jointly impose structural smoothness for each time-step model and smoothness in the structural change for adjacent time-step models.

where $\varphi_d(\mathbf{X})$ is the data misfit or residual-norm functional defined as the difference between the observed and predicted data according to a given p-norm Lp:

$$\varphi_d(\mathbf{X}) = \|\mathbf{Y} - \mathbf{K}\mathbf{X}\|_p. \tag{11}$$

In equation 10, $\varphi_m(\mathbf{X})$ is a stabilizer and α denotes the Tikhonov regularization parameter used to balance or trade off the effects of the two terms in the cost function.

Minimization of equation 10 using the L1 approach is obtained using a model seminorm functional defined by

$$\varphi_m(\mathbf{X}) = (|\mathbf{X}|^2 + \beta^2)^{1/2}, \tag{12}$$

where β is a small number close to zero that provides stability when the model or model gradient is close to zero. The roles and choice of multiple regularization parameters, including the effects of the minimum support parameter β, was discussed by Minsley et al. (2007a, 2007b). One proposed approach to optimizing the choice of β is to generate a set of trade-off curves through repeating an L-curve analysis for increasing values of β. This becomes a tool in selection of an appropriate value for β. However, the choice is still ultimately a subjective one, in that the desired trade-off between compactness and smoothness must be selected based on some a priori information or understanding of the subsurface. For the purposes of this work, we assume knowledge of the approximate shape and size of the target, and we chose a value for β by means of trial and error such that it is small enough as to not cause instabilities in the inversion process but still recovering an adequately compact solution. Here, the solution is algebraically similar to iteratively solving

$$\begin{bmatrix} \mathbf{K} \\ \alpha \mathbf{W_m} \sqrt{\mathbf{R^{k-1}}} \end{bmatrix} [\mathbf{X}] = \begin{bmatrix} \mathbf{Y} \\ \mathbf{0} \end{bmatrix}, \tag{13}$$

where $\mathbf{k}$ denotes the iteration number and $\mathbf{R}$ denotes a diagonal matrix with an entry for differences between adjacent model parameters in all directions and is given by

$$R_{ii} = ((\mathbf{W_m X})_i^2 + \beta^2)^{-1/2}, \tag{14}$$

where $\mathbf{W_m}$ denotes the first order derivative or gradient. At the first iteration, it is convenient to use a linear constraint of $\mathbf{R^0} = \mathbf{I}$, where $\mathbf{I}$ is an identity matrix. The total number of iterations is normally reached when some convergence criterion is reached, such as changes to the model become sufficiently small between adjacent iterations (e.g., $\|\mathbf{X}^k - \mathbf{X}^{k-1}\| < \varepsilon$). In this work, we use a value of $\varepsilon = 2\%$ for the L1 and compact source inversion approaches.

Minimization of equation 10 using the L2 approach (least squares) is a noniterative solution, obtained by using the model seminorm functional,

$$\varphi_m(\mathbf{X}) = \|\mathbf{W_m X}\|_2^2. \tag{15}$$

In this case, the model weighting matrix operator can be defined as $\mathbf{W_m} = \mathbf{I}$ (zero-order derivative), or it can be given by either a first-order derivative (gradient operator) or a second-order derivative (Laplacian operator) depending on the desired structural characteristics of the recovered model. With the inclusion of a depth weighting function $\mathbf{J}$ in the system for 2D surface potential field data, the solution then becomes

$$\begin{bmatrix} \mathbf{J\Omega^{-1}} \\ \alpha \mathbf{I} \end{bmatrix} [\mathbf{X}^*] = \begin{bmatrix} \mathbf{Y} \\ \mathbf{0} \end{bmatrix}, \tag{16}$$

where an efficient way to calculate the depth weighting vector $\mathbf{J}$ is given by the following relationship:

$$\mathbf{J} = \text{diag} \sqrt{\sum_{i=1}^{N} K_{ij}^2}. \tag{17}$$

Here, "diag" refers to a diagonal matrix. This depth weighting of the kernel is aimed at counteracting the sensitivity of the kernel matrix to near-surface model parameters, and it effectively forces the sources to depth within the model space to recover more realistic and meaningful models. Once the weighted model is calculated, it is transformed back to an unscaled parameter set using

$$\mathbf{X} = \mathbf{J^{-1}} \mathbf{X}^*. \tag{18}$$

Finally, in compact source inversion, we seek to find one model with the minimum volume of dipole moments or source currents. As first shown by Last and Kubik (1983) and modified by Minsley et al. (2007a, 2007b) to incorporate depth weighting for potential field problems, the regularizer is given as

$$\varphi_m(\mathbf{X}) = \Omega \int_\Omega \frac{\mathbf{X}^2}{\mathbf{X}^2 + \beta^2}, \tag{19}$$

where Ω denotes the model spatial domain (the sandbox in our case).

In all inversion cases presented herein, an L-curve approach using maximum curvature to selecting an optimal value for the Tikhonov regularization parameter was performed (Hansen and Oleary, 1993). For the case of 3D time-lapse inversion, an additional measure of model seminorm is included into the minimization problem to account for the time-lapse nature of the problem. Here, a first-order derivative operator matrix that measures the change in a given model parameter between adjacent time steps is incorporated into the model seminorm $\varphi_m(\mathbf{X})$. This derivative operator is weighted by a second Tikhonov regularization term defined as $\alpha_2 = \alpha/5$, and it enforces an appropriate amount of smoothness in temporal changes to model structure while still fitting the observed data at each time step.

RESULTS

Results of 3D inversion for source localization

Figure 12 compares the localization results for L1, L2, and compact source 3D inversions showing the recovered 3D vector field of source current density [A · m^{-2}] and calculated magnitude [A · m^{-2}]. Here, the 3D SP data collected throughout the tank were used in the inversions. Although the anomaly recovery for L1 and L2 models are more centered on the x- and y-coordinates of the vertical pipe and reveal some indication of the vertical length of the pipe with relative high-amplitude source current distributions centered at either end or extending from top to bottom of the pipe, the compact source inversion returns a single dominant vertical dipole near the center of the pipe after six iterations. Hence, the compact source inversion results are considered superior specifically for localization purposes. Based on these results, we can see how the three different results are complementary: In a hypothetical

real-world scenario, in which a target object's size and dimensions may be known, but its exact location in space is not known, compact source inversion would be a better approach to localization. However, if the object's location, size, and orientation are unclear, it seems that L1 or L2 approaches would be more appropriate to more fully characterize the target. Figure 13 presents the magnitude of the recovered 3D current density for compact source inversion results plotted as a 3D color contour volume with transparency thresholding. The

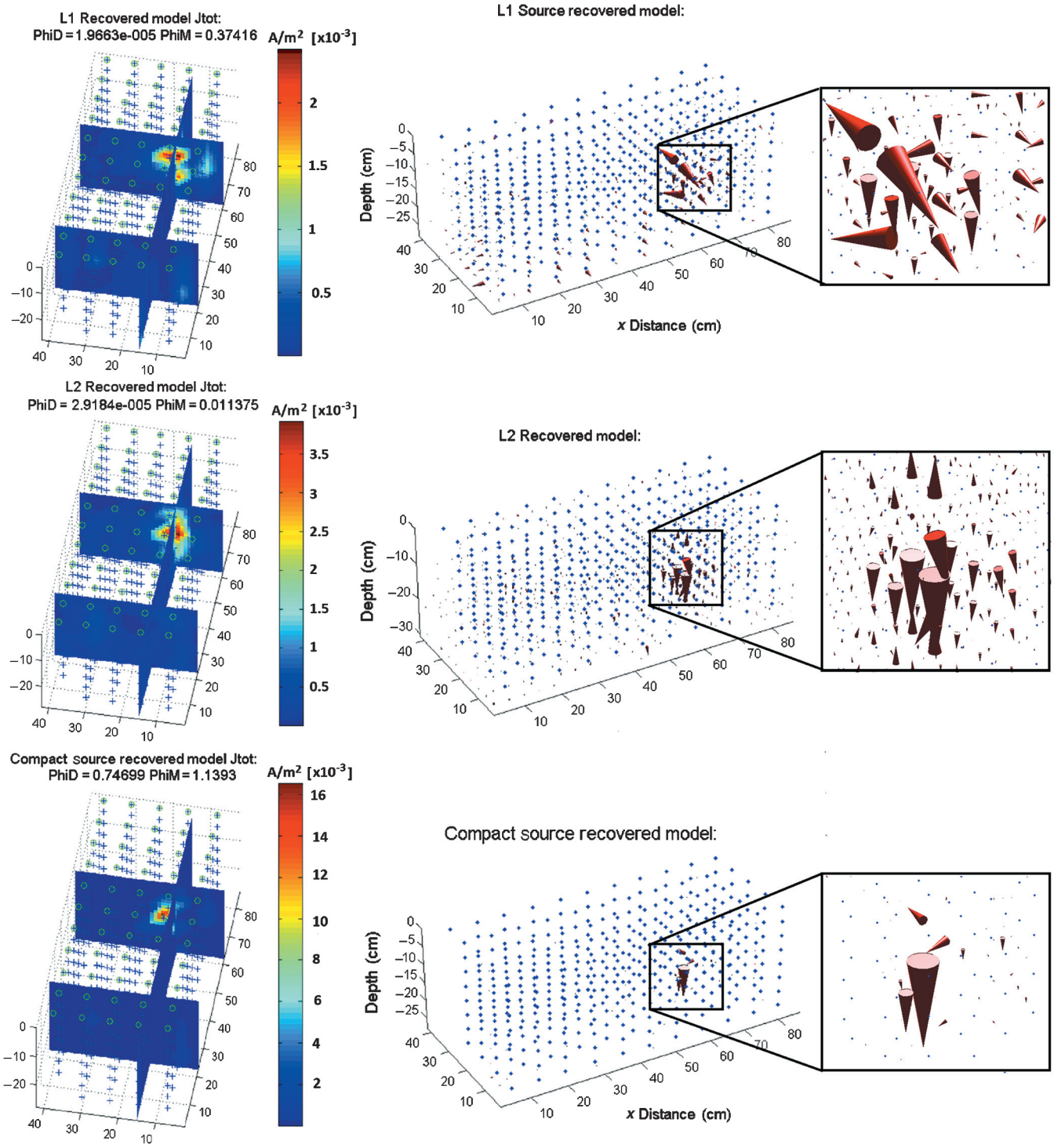

Figure 12. Localization results for L1, L2, and compact source inversions showing the recovered 3D vector field of source current density (right column) with magnified views of the main model localization features recovered to the right, and calculated magnitude of current density in units A/m^2 (left column). Although the anomaly recovery for L1 and L2 models are more centered at the vertical pipe, the compact source inversion returns a single dominant vertical dipole after six iterations.

x- and y-coordinate discrepancy between results is mainly due to the spatial coarseness of the kernel matrix and resultant model parameterization spacing used for this study. The localization could be further refined by creating a more finely meshed kernel matrix in the vicinity of this initial dominant dipole and repeating the compact source inversion using the updated kernel matrix and parameterization spacing similar to the approach taken in Haas et al. (2013).

Based on the results of the localization routine, which show a predominantly vertical current density that is elongated in the z-direction, it was deemed appropriate to further constrain the 4D smooth-model inversion by applying a larger (20%) penalty to x- and y-components of the recovered model vector fields. This is accomplished by decreasing the z-component weights within the minimum-length or "smallest-model" matrix contribution to the final model weighting matrix $\mathbf{W_m}$ during formulation of the model seminorm in equation 15. Additionally, preferential model smoothness in the z-direction was enforced by scaling the z-component of the "smooth-model" matrix contribution to $\mathbf{W_m}$ by a factor of three relative to the x- and y-components. Last, the time-lapse inversions were further constrained by imposing an increasing penalty on recovered source current model parameters with increasing radial distance from the center of the vertical metallic pipe, as determined from the interpretation of localization results. This added constraint helped to ensure that source currents in the recovered model are predominantly in the vicinity of the vertical metallic pipe.

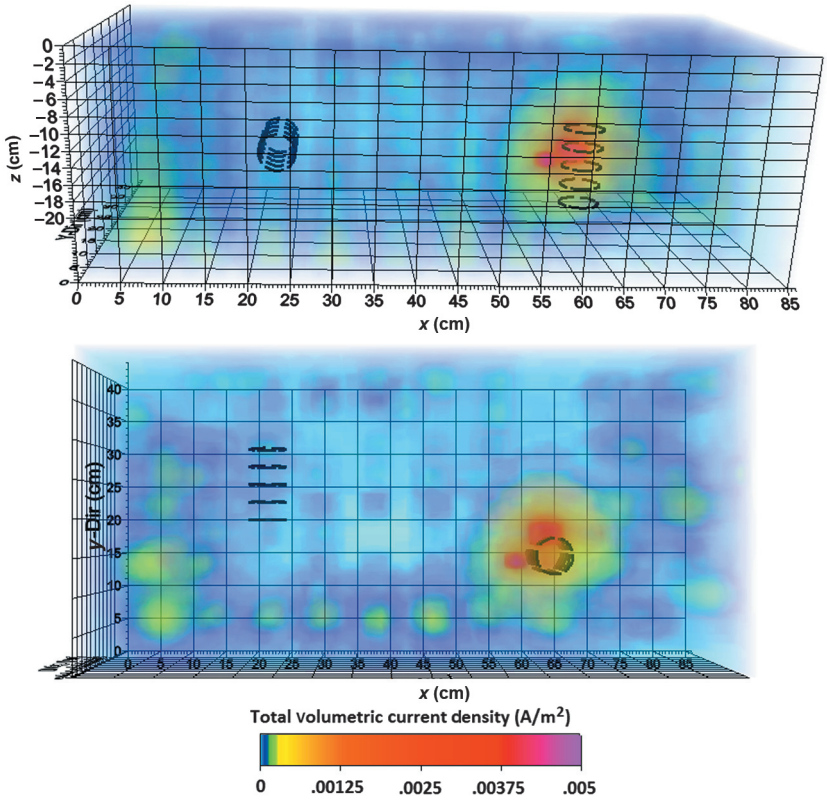

Figure 13. Localization results plotted as a 3D color contour volume of the 3D recovered magnitude of source current density with transparency thresholding for compact source inversion. This inversion result could be used to position and calculate a new refined kernel matrix for further localization refinement.

Results of 4D inversion for E_H distribution

Figure 14 presents 4D SP smooth-model (L2-norm) inversion results, where each column of panels from left to right presents the observed 2D surface SP data, the recovered data, and the magnitude of the recovered source current density distribution calculated using the recovered 3D vector field of source current density distribution, respectively. The progressive development of an SP anomaly associated with the increasing corrosion rate of the vertical metallic pipe is seen over time. Using the L-curve approach to selecting an appropriate regularization term as described by Hansen and Oleary (1993), and imposing smoothness in time with a first-order derivative operator, the recovered current density distribution is seen to fit the observed data well at each time-step but not overfitting the low-magnitude and high spatial-frequency noise.

Finally, the recovered 3D source current model for the last time step is used to calculate the spatial distribution of redox potential in the vicinity of the vertical metallic pipe. Using a discretized representation of the assumed relationship given by $\mathbf{J}_S = -\sigma \nabla E_H$, we recover the E_H distribution by means of a numerical approximation to the 3D spatial integration of the recovered source current density model. Here, we normalize the recovered model of $\mathbf{J}_S$ for the last time step by the 3D distribution of conductivity σ, and we perform a cumulative 3D line integral from the origin of the tank to each model element position sequentially. Because potential data values are relative to some arbitrary common point or value, a linear shift was applied to the recovered E_H data to "ground-truth" or match a measured E_H value near the top of the vertical pipe. Last, these recovered E_H data and the true E_H data were interpolated to selected points along the outer surface of the vertical pipe (Figure 15). Figure 15a compares 3D color scatterplots of the measured and recovered E_H data, and Figure 15b shows a crossplot and calculated coefficient of determination (R^2) value for the measured and recovered E_H distributions. There is good agreement between the measured and recovered E_H distribution at the last time step, demonstrating that SP is useful in qualitatively monitoring the evolution of redox potential gradients at depth in regions where an electronic conductor exists.

POTENTIAL APPLICATIONS

Application to ore bodies and civil engineering

The use of SP in localizing nonintrusively active corrosion processes that are responsible for large quasistatic perturbations to the electric field, and in retrieving the spatial distribution of redox potential within the subsurface, has many implications. This indicates the usefulness of the SP method in the passive monitoring of infrastructure that connecting regions of differing redox potentials in the subsurface. Examples

include bridge columns; drilled shafts and piles containing rebar, rock bolts, and soil anchors; metallic pipelines; and underground cables (e.g., Hubbard et al., 2003; Gucunski et al., 2010). As indicated, for instance, by Sato and Mooney (1960) and Mendonça (2008), this approach to modeling SP data could also be used in detecting and imaging electrically conductive mineral deposits such as disseminated or massive sulfide deposits.

Application to contaminant plumes

Additionally, this study provides insights into the usefulness of the SP method for imaging and monitoring contaminant plumes undergoing biodegradation (Naudet et al., 2003, 2004; Revil et al., 2010), and to potentially aid in the automation of engineered bioremediation efforts. Based on the preliminary works by Naudet et al. (2003, 2004) in the field and in the laboratory, Revil et al. (2010) develop a biogeobattery model, which has been successfully tested by Risgaard-Petersen et al. (2012). As explained in Revil et al. (2009, 2010), it is not sufficient enough to have a redox potential gradient in the ground to generate an SP anomaly, a point that we have emphasized in this paper, but has been missed in earlier studies (see Nyquist and Corry, 2002; Hubbard et al., 2011). There are two possibilities for a biodegraded contaminant plume to contain an electron conductor bridging a strong gradient in the redox potential. The first is the presence of metallic precipitates that are well-documented biodegradation end products at hydrocarbon contaminated

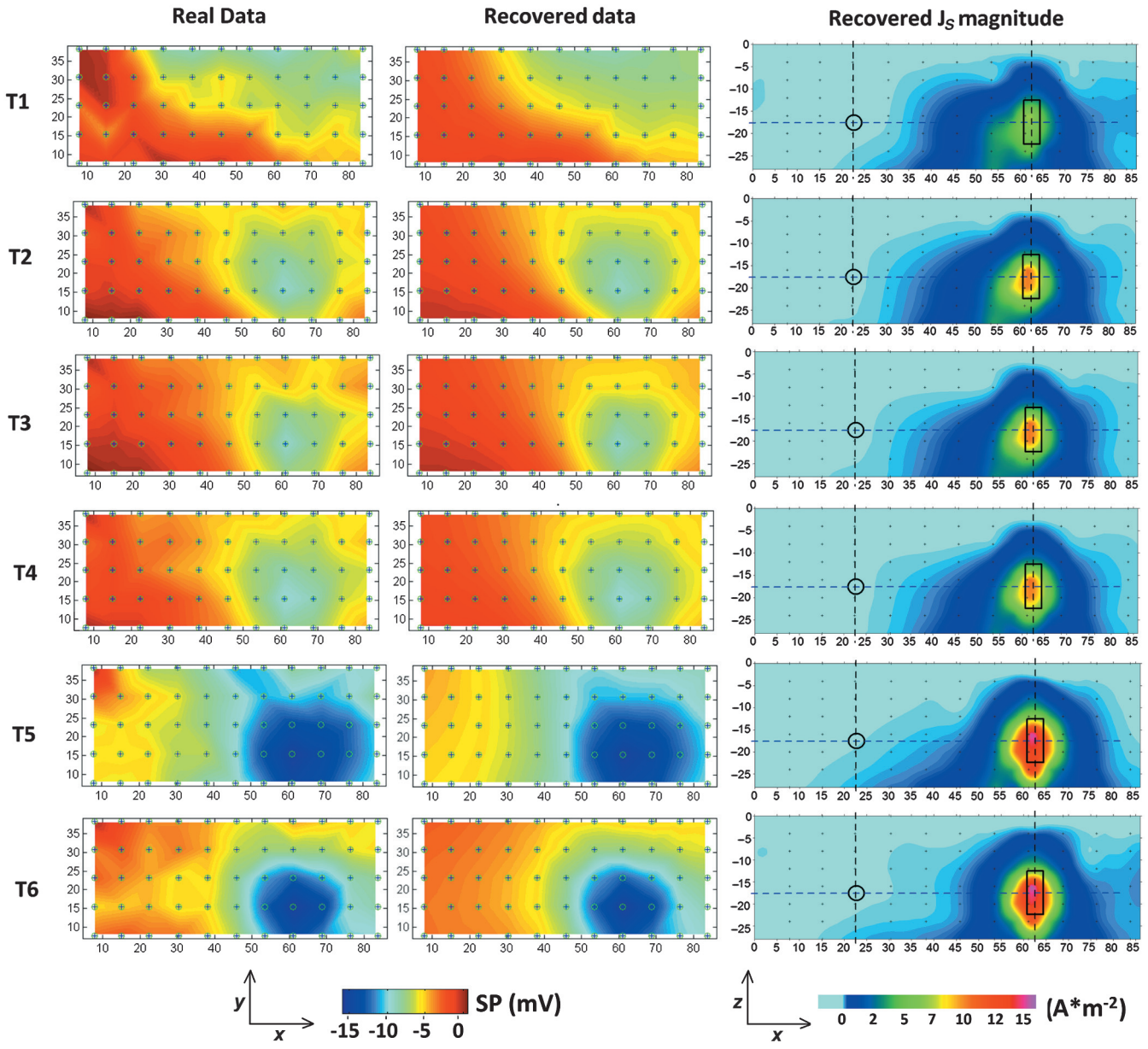

Figure 14. Time-lapse SP modeling results showing color contour plots at each time step (T1 to T6) of the observed (left column) and recovered (center column) 2D surface SP data, and magnitude of the current density distribution (right column) calculated using the recovered 3D vector field source current distribution along a 2D vertical slice ($y = 15$ cm).

sites. The second possibility is that extracellular electron transport occurs along interconnected nanowire networks developed by cells to enhance electron shuttling across redox gradients (see discussion in Revil et al., 2010). These abiotic and biotic conductors may both be present, as shown in Figure 16 and proven experimentally by Kato et al. (2012). Based on this model, Revil et al. (2010) emphasize that a diagnostic, vertically oriented dipolar electrical field must be associated with the presence of a biogeobattery generated by a biodegrading contaminant in the capillary fringe.

Until recently, field-scale evidence of the existence of such a biogeobattery over a mature hydrocarbon contaminated plume was lacking. To test this model, vertical SP monitoring at the National Crude Oil Spill Fate and Natural Attenuation Research Site in Bemidji, Minnesota, is being conducted. In August 1979, a high-pressure crude oil pipeline ruptured, spilling 1,700,000 L of crude oil in an uninhabited area near Bemidji. Oil pooled in low-lying areas (~2000 m^2) and sprayed over an area of 6500 m^2 to the southwest of the pipeline, forming the south and north contaminated plumes. The National Crude Oil Spill Fate and Natural Attenuation Research Site is ideally suited for investigating geobatteries because (1) it is a mature spill site with extensively documented biodegradation (Baedecker et al., 1993; Essaid et al., 2011), (2) the lithology is relatively simple, consisting of ~20-m-thick moderately calcareous sand and glacial outwash deposits overlying clayey till of unknown thickness (Bennett et al., 1993), and (3) a thick (~1 m) layer of oil floats on top of the water table, where a strong redox gradient has developed as a result of long-term biodegradation. Water-table fluctuations at the site have resulted in a well-developed smear zone. Assuming the presence of an electron conductor, excellent conditions for the generation of a biogeobattery (Figure 16) exist at this site.

In June 2010, a ~5-cm diameter corehole (C1010) was drilled at a site on the North Pool, being the largest oil pool at the site, where previous studies indicated that biodegradation is strongest. The corehole was drilled by advancing a core barrel with a polycarbonate liner ahead of a hollow-stem auger to ~15 m below land surface, and about 6 m below the mean water table elevation. An array of 16 nonpolarizing Petiau Pb-PbCl electrodes (Petiau, 2000) was built by attaching the electrodes to 3.8-cm-diameter PVC pipe, with connecting wires extending along the pipe to the surface. Electrodes were spaced at 1-m intervals from land surface, with an additional electrode at 7.5 m, close to the center of the smear zone. The electrode array was installed in the hole immediately after drilling, and the hole was backfilled using a slurry of the native material produced during drilling. SPs were recorded using a high-impedance (100 MΩ) voltmeter with the uppermost electrode at 1-m depth assigned as the reference electrode and connected to the negative terminal of the voltmeter by convention. Data sets were acquired on a monthly basis from June 2010 to June 2012.

SP data acquired on this vertical array of electrodes are shown in Figure 17. The existence of a dipolar anomaly (peak-to-peak voltages up to 64 mV, very similar in magnitude to that shown in our laboratory experiment) provides compelling evidence of the existence of a geobattery at this site. The dipole of the geobattery is centered on a 2-m-wide, high mass-magnetic susceptibility interval that defines the smear zone, and is the response of iron oxides, primarily magnetite, that are long-term biodegradation end products precipitated in the smear zone (Mewafy et al., 2011). These iron mineral precipitates provide the required electron conductor: This electron conduction is possibly enhanced by cells as suggested in Figure 16. The coupled redox reactions that drive the electron transport are currently uncertain. In addition to being an anaerobic to aerobic redox transition as in our tank experiments, other redox couples associated with iron reduction also exist in the vadose zone at this site. Furthermore, the data shown in Figure 17 seem to indicate that the geobattery may be transient depending on the position of the water

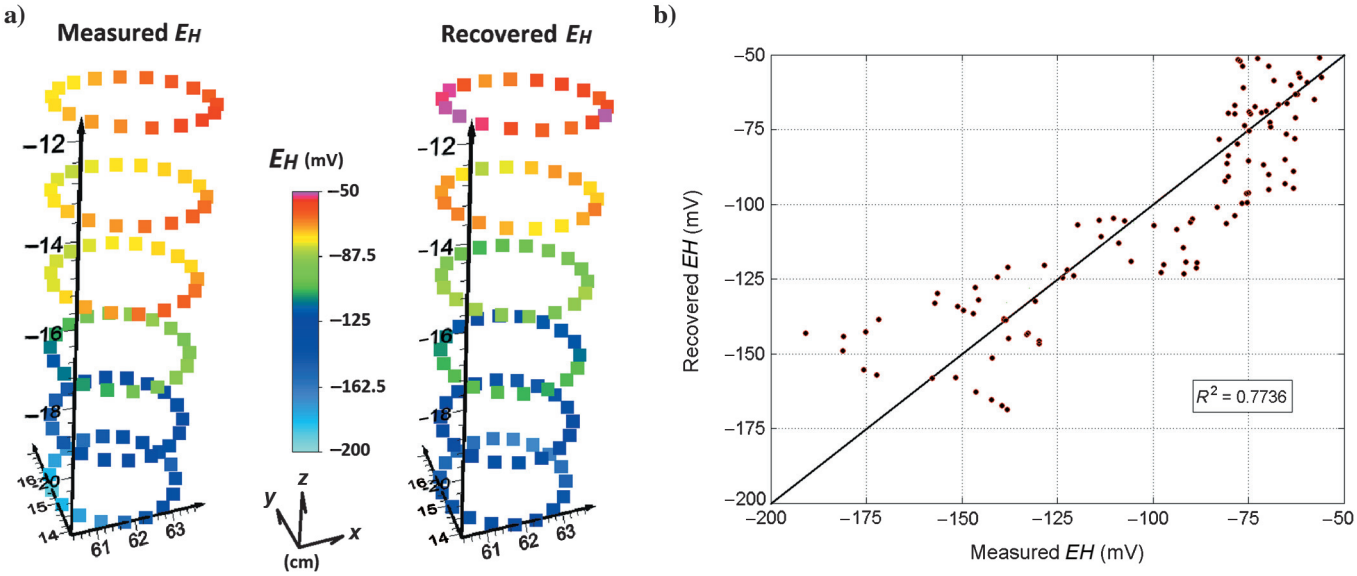

Figure 15. Redox potential (E_H) results: 3D color scatterplots of the measured and recovered E_H distributions as interpolated to select points along the outer surface of the vertical metallic pipe (a), and a crossplot of the measured and recovered E_H data with calculated R^2 coefficient of determination (b). The recovered E_H data were calculated using the recovered model for SP data collected at the last time-step of experiment 2 (Figure 13), and the measured E_H data were collected at the same time-step (see Figure 8). The main discrepancy between the observed and recovered E_H distributions near the center of the pipe (at the phreatic) is likely due to the relative spatial coarseness of model parameterization, resulting in interpolation between nonideally located dipoles in the immediate vicinity of the vertical pipe.

table relative to the position of the high concentration in magnetite. Here, the peak-to-peak magnitude of the dipolar SP anomaly is seen to generally increase as the phreatic surface is lowered. Similar to the laboratory tank experiments presented here, lowering of the phreatic surface at the Bemidji site likely results in a nonlinear increase in the observed geobattery kinetics due to a significant increase in the vertical water saturation gradient and associated vertical dissolved oxygen concentration and vertical aerobic redox gradients across the precipitated magnetite interval. Furthermore, the nonlinear nature of this transient behavior may be the result of local perturbations to the redox potential distribution below the contaminant plume, as observed in the vicinity below the vertical metallic pipe the laboratory experiment 2. This hypothesis could be further corroborated by correlating precipitation and surface water infiltration rates with observed SP data at the site, as well as monitoring the vertical redox potential distributions above and below the magnetite interval within the vicinity of corehole C1010. Further research is being conducted to determine the redox couples driving this geobattery, to determine the potential role of bacteria in facilitating the electron transport observed with SP at this site, and to understand the kinetics of the geobattery with respect to the change of elevation of the water table.

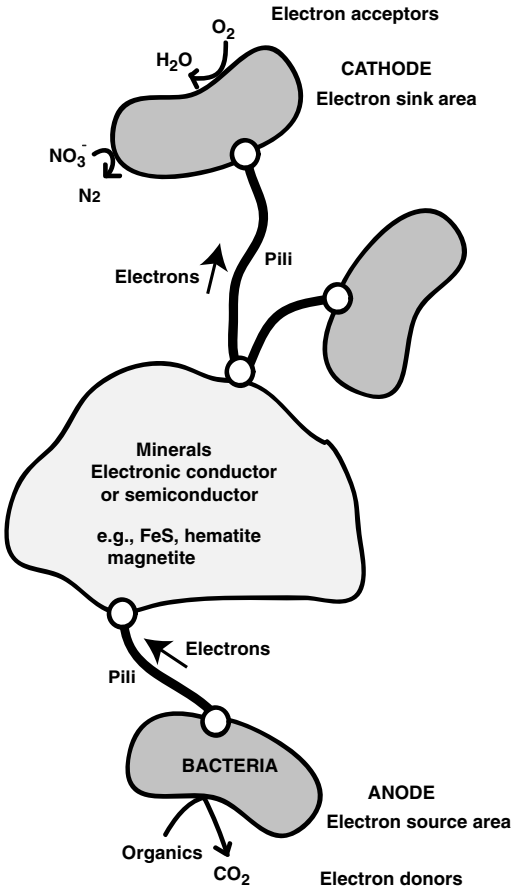

Figure 16. Possible electron transfer mechanisms in the capillary fringe of a contaminant plume. The presence of metallic minerals resulting from biological activity and bacteria populations connected by conductive pili favor the transfer of electrons through the capillary fringe. At the "bacterial anode," electrons are gained through the oxidation of the organic matter, iron oxides, or Fe-bearing phyllosilicates. The electrons are conveyed to the "bacterial cathode" through a network of conductive pili and metallic particles. At the bacterial cathode, oxygen and nitrate prevail as electron acceptors. In this system, bacteria act as catalysts. The transport of electrons through the anode to the cathode of the microbattery may involve different bacterial communities and different electron transfer mechanisms including external electron shuttles (modified from Revil et al., 2010).

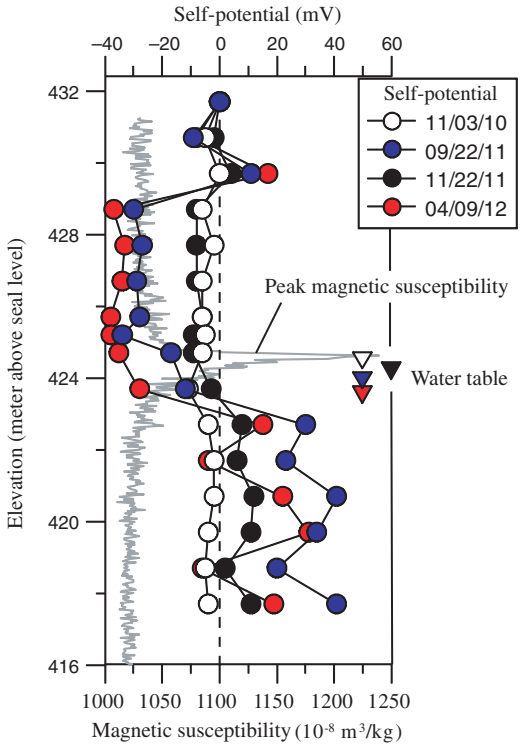

Figure 17. Vertical SP data showing the development of a dipolar anomaly at the capillary fringe above a contaminant plume associated with the oil spill of Bemidji in Minnesota. Compare the dipolar anomaly to Figure 7 in polarity and magnitude. The position of the dipolar anomaly is just below the peak in the concentration in magnetite and corresponds to the position of the water table (see inverted triangles on the right side of the figure).

CONCLUSIONS

The following conclusions have been reached in this paper:

1) To produce an SP anomaly associated with a redox potential gradient, an electronic conductor has to intercept an area of strong redox potential gradient. For instance, a metallic body or biotic conductor network needs to cross the capillary fringe to generate a strong SP anomaly. Using two types of sands with two different grain sizes, and therefore two different thickness of the capillary fringe, we have observed two different values and spatial distributions of the resulting SP signals. If the metallic body is localized in the capillary fringe but it is not exposed to a strong enough redox potential gradient, the resulting SP anomaly is vanishingly small.
2) The generation of an electrical current in the metallic material is associated with the corrosion of the metallic material and the formation of an SP anomaly. The corrosion modifies the conductivity distribution (by forming a resistive crust on the surface

of the metallic object) and the distribution of the redox potential in the vicinity of the metallic object, creating nonlinear corrosion kinetics due to positive feedback and subsequent passivation phenomena.

3) Due to the relationship between corrosion and the SP anomaly, the time-lapse inversion of the SP signals can be used to nonintrusively monitor the progress of corrosion. Numerous applications can be foreseen in terms of using this novel approach in civil engineering, for instance, for the detection/localization of corroded rebar in armed concrete or in mining for the localization of ore bodies.
4) Noted consistencies between the sand tank experiments data and the Bemidji field data and observations provide indication for the presence of a biogeobattery over biodegrading light hydrocarbon contaminant plumes floating on the water table, assuming the existence of an electronic conductor.
5) The kinetics of the geobatteries observed in the laboratory data and Bemidji field data appears to be clearly transient and strongly dependent on the elevation of the phreatic surface and the vertical water-saturation profile relative to the position of an electronic conductor. As seen in the Bemidji field data, seasonal variation in the elevation of the phreatic surface due to the infiltration of meteoric water clearly influences the magnitude of the associated SP anomaly. Similarly, the shape of the water-saturation curve and related dissolved oxygen concentrations within the capillary fringe of the laboratory experiments have been shown to significantly influence the magnitude and spatial extent of the observed SP anomalies. Similar to observations made in experiment 2, the nonlinear relationship between the peak-to-peak magnitude of the Bemidji SP anomaly with respect to the phreatic surface elevation fluctuations is likely due to local perturbations of the redox potential distribution in the vicinity of the contaminant plume.

ACKNOWLEDGMENTS

We thank the NSF for funding the SmartGeo Educational Program (Project IGERT: Intelligent Geosystems; DGE-0801692). Thanks go to P. Sava and T. Young for their generous encouragements and support at Mines. This material is partially based on work supported by Enbridge Energy (Ltd.), the Minnesota Pollution Control Agency, and the U.S.G.S. Toxic Waste Substances Program. We also thank Chevron Energy Technology Company (grants CW852844 and K26625). Funding for the Bemidji project was provided by the Minnesota Pollution Control Agency and the U.S.G.S. Toxic Substances Hydrology Program.

APPENDIX A

FAR-FIELD DIPOLAR APPROXIMATION

We use a multipole expansion of the electrostatic potential in the far-field of a corroding metallic object. We first consider an infinite homogeneous conductive material in 3D. We consider situations in which the electrodes are far enough from the metallic object to treat the source of current associated with corrosion as a point source. The multipole expansion of the electrical potential represents the expansion of the electrical potential distribution in successive power of $(1/r)$, where r is the distance between the source and the electrode located at position $\mathbf{r}$:

$$\varphi(\mathbf{r}) = \frac{1}{4\pi\sigma}\sum_{n=0}^{\infty}\frac{1}{r^{n+1}}\int_{\Omega}(\mathbf{r}')^n P_n(\cos\,\theta')\Im(\mathbf{r}')\mathrm{d}V', \quad \text{(A-1)}$$

where Ω is the source volume in which the current sources exist; $P_n(x)$ are Legendre polynomials; and θ' is the angle between the two vectors $\mathbf{r}$ and $\mathbf{r}'$, where $\mathbf{r}'$ corresponds to the position of the source in a Cartesian framework. In the following, we note this expansion as

$$\varphi(\mathbf{r}) = \varphi^0(\mathbf{r}) + \varphi^1(\mathbf{r}) + \varphi^2(\mathbf{r}) + \cdots . \quad \text{(A-2)}$$

Here, $\varphi^0(\mathbf{r})$ represents the monopole term, $\varphi^1(\mathbf{r})$ is the dipole term, $\varphi^2(\mathbf{r})$ is the quadrupole term, and so on. If r is large, the expansion is dominated by the first term:

$$\varphi^0(\mathbf{r}) = \frac{1}{4\pi\sigma}\frac{1}{r}\int_{\Omega}\Im(\mathbf{r}')\mathrm{d}V', \quad \text{(A-3)}$$

$$\varphi^0(\mathbf{r}) = \frac{1}{4\pi\sigma}\frac{I_S}{r}, \quad \text{(A-4)}$$

where the total current I_S corresponds to the moment of order 1 of the volumetric current distribution $\Im(\mathbf{r}')$:

$$I_S = \int_{\Omega}\Im(\mathbf{r}')\mathrm{d}V' = \int_{\Omega}\nabla\cdot\mathbf{J}_S\mathrm{d}V', \quad \text{(A-5)}$$

$$I_S = \int_{\partial\Omega}\mathbf{J}_S\cdot\mathrm{d}\mathbf{a}. \quad \text{(A-6)}$$

Here, we have used the divergence theorem, where $d\mathbf{a}$ is the surface element of the interface $\partial\Omega$ pointing outward and normal to the surface of the volume Ω. The charge conservation equation implies that the integral in equation A-6 vanishes (there is no charge storage inside the volume associated with the flow of the electrons in the metallic object; see Figure 10). Therefore, the monopole term of the multipole expansion series is equal to zero. It follows that the leading term is the dipolar term given by

$$\varphi^1(\mathbf{r}) = -\frac{1}{4\pi\sigma}\frac{1}{r^2}\int_{\Omega}\mathbf{r}'\cos\,\theta'\Im(\mathbf{r}')\mathrm{d}V'. \quad \text{(A-7)}$$

If we note $\hat{\mathbf{r}}$ the unit vector between the origin of the Cartesian coordinate system and the observation point P, we have $\hat{\mathbf{r}}\cdot\mathbf{r}' = \mathbf{r}'\cos\,\theta'$. This yields

$$\varphi^1(\mathbf{r}) = \frac{1}{4\pi\sigma}\frac{1}{r^2}\hat{\mathbf{r}}\cdot\int_{\Omega}\mathbf{r}'\Im(\mathbf{r}')\mathrm{d}V'. \quad \text{(A-8)}$$

The dipole moment is the second-order moment of the charge distribution. It is given by

$$\mathbf{d} = \int_{\Omega}\mathbf{r}'\Im(\mathbf{r}')\mathrm{d}V'. \quad \text{(A-9)}$$

We can use this approximation and a parametric approach to find the position of the metallic object in the tank using this far-field dipole approximation.

REFERENCES

Arora, T., N. Linde, A. Revil, and J. Castermant, 2007, Non-intrusive determination of the redox potential of contaminant plumes by using the self-potential method: Journal of Contaminant Hydrology, **92**, 274–292, doi: 10.1016/j.jconhyd.2007.01.018.

Baedecker, M. J., I. M. Cozzarelli, R. P. Eganhouse, D. I. Siegel, and P. C. Bennett, 1993, Crude oil in a shallow sand and gravel aquifer: III. Biogeochemical reactions and mass balance modeling in anoxic groundwater: Applied Geochemistry, **8**, 569–586, doi: 10.1016/0883-2927(93)90014-8.

Bennett, P. C., D. E. Siegel, M. J. Baedecker, and M. F. Hult, 1993, Crude oil in a shallow sand and gravel aquifer: I. Hydrogeology and inorganic geochemistry: Applied Geochemistry, **8**, 529–549, doi: 10.1016/0883-2927(93)90012-6.

Birch, F. S., 1998, Imaging the water table by filtering self-potential profiles: Ground Water, **36**, 779–782, doi: 10.1111/j.1745-6584.1998.tb02195.x.

Bolève, A., A. Revil, F. Janod, J. L. Mattiuzzo, and J. Fry, 2009, Preferential fluid flow pathways in embankment dams imaged by self-potential tomography: Near Surface Geophysics, **7**, 447–462, doi: 10.3997/1873-0604.2009012.

Bolève, A., A. Revil, F. Janod, J. L. Mattiuzzo, and A. Jardani, 2007, Forward modeling and validation of a new formulation to compute self-potential signals associated with ground water flow: Hydrology and Earth System Sciences, **11**, 1661–1671, doi: 10.5194/hess-11-1661-2007.

Byrdina, S., S. Friedel, J. Wassermann, and J. Zlotnicki, 2003, Self-potential variations associated with ultra-long period seismic signals at Merapi Volcano: Geophysical Research Letters, **30**, 2156, doi: 10.1029/2003GL018272.

Castermant, J., C. A. Mendonça, A. Revil, F. Trolard, G. Bourrié, and N. Linde, 2008, Redox potential distribution inferred from self-potential measurements associated with the corrosion of a burden metallic body: Geophysical Prospecting, **56**, 269–282, doi: 10.1111/j.1365-2478.2007.00675.x.

Crespy, A., A. Revil, N. Linde, S. Byrdina, A. Jardani, A. Bolève, and P. Henry, 2008, Detection and localization of hydromechanical disturbances in a sandbox using the self-potential method: Journal of Geophysical Research, **113**, B01205, doi: 10.1029/2007JB005042.

Doherty, R., B. Kulessa, A. S. Ferguson, M. J. Larkin, L. A. Kulakov, and R. M. Kalin, 2010, A microbial fuel cell in contaminated ground delineated by electrical self-potential and normalized induced polarization data: Journal of Geophysical Research, **113**, B01205, doi: 10.1029/2007JB005042.

Essaid, H. I., B. A. Bekins, W. N. Herkelrath, and G. N. Delin, 2011, Crude oil at the Bemidji Site: 25 years of monitoring, modeling, and understanding: Ground Water, **49**,706–726, doi: 10.1111/j.1745-6584.2009.00654.x.

Fachin, S. J. S., E. L. Abreu, C. A. Mendonça, A. Revil, G. C. Novaes, and S. S. Vasconcelos, 2012, Self-potential signals from an analog biogeobattery model: Geophysics, **77**, no. 4, EN29–EN37, doi: 10.1190/geo2011-0352.1.

Farquharson, C. G., and D. W. Oldenburg, 1998, Nonlinear inversion using general measures of data misfit and model structure: Geophysical Journal International, **134**, 213–227, doi: 10.1046/j.1365-246x.1998.00555.x.

Finizola, A., F. Sortino, J. Lenat, and M. Valenza, 2002, Fluid circulation at Stromboli volcano (Aeolian Islands, Italy) from self-potential and CO_2 surveys: Journal of Volcanology and Geothermal Research, **116**, 1–18, doi: 10.1016/S0377-0273(01)00327-4.

Gorby, Y. A., S. Yanina, J. S. McLean, K. M. Rosso, D. Moyles, and A. Dohnalkova, 2006, Electrically conductive bacterial nanowires produced by *Shewanella oneidensis* strain MR-1 and other microorganisms: Proceedings of the National Academy of Sciences of the United States of America, **103**, 11358–11363, doi: 10.1073/pnas.0604517103.

Gucunski, N., F. Romero, S. Kruschwitz, R. Feldmann, A. Abu-Hawash, and M. Dunn, 2010, Multiple complementary nondestructive evaluation technologies for condition assessment of concrete bridge decks: Transportation Research Record, **2201**, 34–44, doi: 10.3141/2201-05.

Haas, A. K., A. Revil, M. Karaoulis, L. Frash, J. Hampton, M. Gutierrez, and M. Mooney, 2013, Electrical potential source localization reveal a borehole leak during hydraulic fracturing: Geophysics, **78**, no. 2, D93–D113, doi: 10.1190/geo2012-0388.1.

Hansen, P. C., and D. Oleary, 1993, The use of the L-curve in the regularization of discrete ill-posed problems: Journal of Scientific Computing, **14**, 1487–1503, doi: 10.1137/0914086.

Hubbard, C. G., L. J. West, K. Morris, B. Kulessa, D. Brookshaw, J. R. Lloyd, and S. Shaw, 2011, In search of experimental evidence for the biogeobattery: Journal of Geophysical Research, **116**, G04018, doi: 10.1029/2011JG001713.

Hubbard, S. S., J. Y. Zhang, P. J. M. Monteiro, J. E. Peterson, and Y. Rubin, 2003, Experimental detection of reinforcing bar corrosion using nondestructive geophysical techniques: ACI Materials Journal, **100**, 501–510.

Ikard, S. J., A. Revil, A. Jardani, W. F. Woodruff, M. Parekh, and M. Mooney, 2012, Saline pulse test monitoring with the self-potential method to non-intrusively determine the velocity of the pore water in leaking areas of earth dams and embankments: Water Resources Research, **48**, W04201, doi: 10.1029/2010WR010247.

Jardani, A., and A. Revil, 2009, Stochastic joint inversion of temperature and self-potential data: Geophysical Journal International, **179**, 640–654, doi: 10.1111/j.1365-246X.2009.04295.x.

Jardani, A., A. Revil, F. Akao, M. Schmutz, N. Florsch, and J. P. Dupont, 2006, Least squares inversion of self-potential (SP) data and application to the shallow flow of ground water in sinkholes: Geophysical Research Letters, **33**, L19306, doi: 10.1029/2006GL027458.

Jardani, A., A. Revil, W. Barrash, A. Crespy, E. Rizzo, S. Straface, M. Cardiff, B. Malama, C. Miller, and T. Johnson, 2009, Reconstruction of the water table from self-potential data: A Bayesian approach: Ground Water, **47**, 213–227, doi: 10.1111/j.1745-6584.2008.00513.x.

Jardani, A., A. Revil, A. Bolève, A. Crespy, J. P. Dupont, and W. Barrash, 2007a, Tomography of Darcy velocity from self-potential measurements: Geophysical Research Letters, **34**, L24403, doi: 10.1029/2007GL031907.

Jardani, A., A. Revil, A. Bolève, and J. P. Dupont, 2008, 3D inversion of self-potential data used to constrain the pattern of ground water flow in geothermal fields: Journal of Geophysical Research, **113**, B09204, doi: 10.1029/2007JB005302.

Jardani, A., A. Revil, F. Santos, C. Fauchard, and J. P. Dupont, 2007b, Detection of preferential infiltration pathways in sinkholes using joint inversion of self-potential and EM-34 conductivity data: Geophysical Prospecting, **55**, 749–760, doi: 10.1111/j.1365-2478.2007.00638.x.

Karaoulis, M., J.-H. Kim, and P. I. Tsourlos, 2011a, 4D active time constrained inversion: Journal of Applied Geophysics, **73**, 25–34, doi: 10.1016/j.jappgeo.2010.11.002.

Karaoulis, M., A. Revil, D. D. Werkema, B. Minsley, W. F. Woodruff, and A. Kemna, 2011b, Time-lapse 3D inversion of complex conductivity data using an active time constrained (ATC) approach: Geophysical Journal International, **187**, 237–251, doi: 10.1111/j.1365-246X.2011.05156.x.

Kato, S., K. Hashimoto, and K. Watanabe, (2012), Microbial interspecies electron transfer via electric currents through conductive minerals: Proceedings of the National Academy of Sciences of the United States of America, **109**, 10042–10046, doi: 10.1073/pnas.1117592109.

Last, B. J., and K. Kubik, 1983, Compact gravity inversion: Geophysics, **48**, 713–721, doi: 10.1190/1.1441501.

Linde, N., and A. Revil, 2007, Tomography inverting self-potential data for redox potentials of contaminant plumes: Geophysical Research Letters, **34**, L14302, doi: 10.1029/2007GL030084.

Maineult, A., E. Strobach, and J. Renner1t, 2008, Self-potential signals induced by periodic pumping tests: Journal of Geophysical Research, **113**, B01203, doi: 10.1029/2007JB005193.

Martínez-Pagán, P., A. Jardani, A. Revil, and A. Haas, 2010, Self-potential monitoring of a salt plume: Geophysics, **75**, no. 4, WA17–WA25, doi: 10.1190/1.3475533.

Mendonça, C. A., 2008, Forward and inverse self-potential modeling in mineral exploration: Geophysics, **73**, no. 1, F33–F43, doi: 10.1190/1.2821191.

Mewafy, F. M., E. A. Atekwana, D. D. Werkema Jr., L. D. Slater, D. Ntarlagiannis, A. Revil, M. Skold, and G. N. Delin, 2011, Magnetic susceptibility as a proxy for investigating microbially mediated iron reduction: Geophysical Research Letters, **38**, L21402, doi: 10.1029/2011GL049271.

Minsley, B. J., J. Sogade, and F. D. Morgan, 2007a, Three-dimensional self-potential inversion for subsurface DNAPL contaminant detection at the Savannah River Site, South Carolina: Water Resources Research, **43**, W04429, doi: 10.1029/2005WR003996.

Minsley, B. J., J. Sogade, and F. D. Morgan, 2007b, Three-dimensional source inversion of self-potential data: Journal of Geophysical Research, **112**, B02202, doi: 10.1029/2006JB004262.

Moore, J. R., and S. D. Glaser, 2007, Self-potential observations during hydraulic fracturing: Journal of Geophysical Research, **112**, B02204, doi: 10.1029/2006JB004373.

Naudet, V., and A. Revil, 2005, A sandbox experiment of the relationship between redox and self-potential and its application to the interpretation of self-potential data over contaminant plumes: Geophysical Research Letters, **32**, L11405, doi: 10.1029/2005GL022735.

Naudet, V., A. Revil, and J. Y. Bottero, 2003, Relationship between self-potential (self-potential) signals and redox conditions in contaminated

groundwater: Geophysical Research Letters, **30**, 2091, doi: 10.1029/2003GL018096.
Naudet, V., A. Revil, E. Rizzo, J. Y. Bottero, and P. Begassat, 2004, Groundwater redox conditions and conductivity in a contaminant plume from geoelectric investigations: Hydrology and Earth System Sciences, **8**, 8–22, doi: 10.5194/hess-8-8-2004.
Ntarlagiannis, D., E. Atekwana, E. Hill, and Y. Gorby, 2007, Microbial nanowires: Is the subsurface 'hardwired'?: Geophysical Research Letters, **34**, L17305, doi: 10.1029/2007GL030426.
Nyquist, J. E., and C. E. Corry, 2002, Self-potential: The ugly duckling of environmental geophysics: The Leading Edge, **21**, 446–451, doi: 10.1190/1.1481251.
Onuma, K., J. Muto, H. Nagahama, and K. Otsuki, 2011, Electric potential changes associated with nucleation of stick-slip of simulated gouges: Tectonophysics, **502**, 308–314, doi: 10.1016/j.tecto.2011.01.018.
Perrier, F., G. Petiau, G. Clerc, V. Bogorodsky, and E. Erkul, 1997, A one-year systematic study of electrodes for long period measurements of the electric field in geophysical environments: Journal of Geomagnetism and Geoelectricity, **49**, 1677–1696, doi: 10.5636/jgg.49.1677.
Petiau, G., 2000, Second generation of lead-lead chloride electrodes for geophysical applications: Pure and Applied Geophysics, **157**, 357–382, doi: 10.1007/s000240050004.
Revil, A., L. Ehouarne, and E. Thyreault, 2001, Tomography of self-potential anomalies of electrochemical nature: Geophysical Research Letters, **28**, 4363–4366, doi: 10.1029/2001GL013631.
Revil, A., A. Finizola, F. Sortino, and M. Ripepe, 2004, Geophysical investigations at Stromboli volcano, Italy. Implications for ground water flow and paroxysmal activity: Geophysical Journal International, **157**, 426–440.
Revil, A., and A. Jardani, 2010, Stochastic inversion of permeability and dispersivities from time lapse self-potential measurements: A controlled sandbox study: Geophysical Research Letters, **37**, L11404, doi: 10.1029/2010GL043257.
Revil, A., M. Karaoulis, T. Johnson, and A. Kemna, 2012, Review: Some low-frequency electrical methods for subsurface characterization and monitoring in hydrogeology: Hydrogeology Journal, **20**, 617–658, doi: 10.1007/s10040-011-0819-x.
Revil, A., C. A. Mendonça, E. Atekwana, B. Kulessa, S. S. Hubbard, and K. Bolhen, 2010, Understanding biogeobatteries: Where geophysics meets microbiology: Journal of Geophysical Research, **115**, G00G02, doi: 10.1029/2009JG001065.
Revil, A., V. Naudet, J. Nouzaret, and M. Pessel, 2003, Principles of electrography applied to self-potential electrokinetic sources and hydrogeological applications: Water Resources Research, **39**, doi: 10.1029/2001WR000916.
Revil, A., F. Trolard, G. Bourrié, J. Castermant, A. Jardani, and C. A. Mendonça, 2009, Ionic contribution to the self-potential signals associated with a redox front: Journal of Contaminant Hydrology, **109**, 27–39, doi: 10.1016/j.jconhyd.2009.07.008.
Revil, A., W. F. Woodruff, and N. Lu, 2011, Constitutive equations for coupled flows in clay materials: Water Resources Research, **47**, W05548, doi: 10.1029/2010WR010002.
Richards, K., A. Revil, A. Jardani, F. Henderson, M. Batzle, and A. Haas, 2010, Pattern of shallow ground water flow at Mount Princeton Hot Springs, Colorado, using geoelectrical methods: Journal of Volcanology and Geothermal Research, **198**, 217–232, doi: 10.1016/j.jvolgeores.2010.09.001.
Risgaard-Petersen, N., A. Revil, P. Meister, and L. P. Nielsen, 2012, Sulfur, iron-, and calcium cycling associated with natural electric currents running through marine sediment: Geochimica et Cosmochimica Acta, **92**, 1–13, doi: 10.1016/j.gca.2012.05.036.
Sakaki, T., and M. Komatsu, 2007, Physical and hydraulic properties of silica sands for laboratory experiments: Colorado School of Mines, unpublished laboratory studies report.
Sato, M., and H. M. Mooney, 1960, The electrochemical mechanism of sulfide self-potentials: Geophysics, **25**, 226–249, doi: 10.1190/1.1438689.
Sheffer, M. R., 2007, Forward modelling and inversion of streaming potential for the interpretation of hydraulic conditions from self-potential data: Ph.D. thesis, University of British Columbia.
Timm, F., and P. Möller, 2001, The relation between electrical and redox potential: Evidence from laboratory and field measurements: Journal of Geochemical Exploration, **72**, 115–128, doi: 10.1016/S0375-6742(01)00157-1.
Trujillo-Barreto, N. J., E. Aubert-Vásquez, and P. A. Valdès-Sosa, 2004, Bayesian model averaging in EEG-MEG imaging: NeuroImage, **21**, 1300–1319, doi: 10.1016/j.neuroimage.2003.11.008.
Yasukawa, K., T. Ishido, and I. Suzuki, 2005, Geothermal reservoir monitoring by continuous self-potential measurements, Mori geothermal field, Japan: Geothermics, **34**, 551–567, doi: 10.1016/j.geothermics.2005.04.005.